

Integration of III-V Microscale Light-Emitting Diodes for Cell-Sized Optical Wireless Electronics

CNF Project Number: 900-00

Principal Investigator(s): Paul L. McEuen^{1,2}

User(s): Yanxin Ji³, Alejandro J. Cortese¹, Conrad Smart¹

Affiliation(s): 1. Laboratory of Atomic and Solid State Physics, 2. Kavli Institute at Cornell for Nanoscale Science, 3. Electrical and Computer Engineering; Cornell University

Primary Source(s) of Research Funding: Cornell Center for Materials Research with funding from the NSF MRSEC program (DMR-1719875), Air Force Office of Scientific Research (AFSOR) multidisciplinary research program of the university research initiative Grant FA2386.13-1-4118

Contact: plm23@cornell.edu, yj323@cornell.edu, ajc383@cornell.edu, cs2239@cornell.edu

Primary CNF Tools Used: Odd hour evaporator, ABM contact aligner, Oxford 81 etcher, AJA sputter deposition tool, P10 profilometer, RTA-AG610, Heidelberg mask writer DWL2000

Abstract:

Opto-electric circuits comprising light emitting diodes, photovoltaic cells, electric circuits etc. have attracted increasing attention and have found broad applications in fields ranging from displays to bio-integrated systems. A transfer technique to integrate optical and electrical devices together is required. Here we present a 4-inch wafer-scale aligned transfer method for integrating micro-LEDs with silicon circuits. This method demonstrates both high transfer yield and high alignment accuracy.

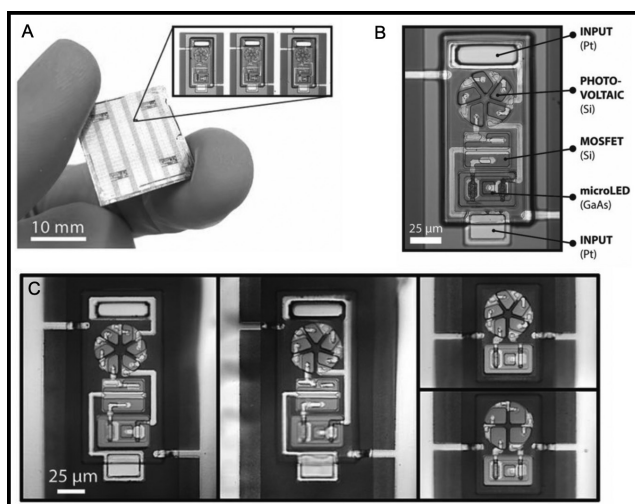


Figure 1: (A) Image of a chip containing thousands of integrated optical wireless integrated circuit (OWIC) sensors. (B) Optical image of an OWIC sensor with components labeled. (C) Image of various OWIC sensors with different functions.

Summary of Research:

Inorganic microscale light-emitting diodes (micro-LEDs) are broadly used in optoelectronic systems because of their high efficiency, color purity and reliability. Our group has recently developed a platform combining both inorganic micro-LEDs and electric circuits: optical

wireless integrated circuits (OWICs) [1] (Figure 1). The OWIC sensors are approximately 100 μm across, which is microscopic in size, and can be used for a wide range of applications such as biosensing.

To integrate the micro-LEDs and silicon-based devices into the same circuit, a challenge must be met: high quality inorganic micro-LEDs are commonly grown on non-silicon substrates such as gallium arsenide (GaAs), while the electric circuits are fabricated on silicon substrates. Therefore, effective transfer methods are required. We develop an approach for transferring GaAs micro-LEDs from their native substrates to silicon substrate at wafer scale.

The micro-LEDs are fabricated on a commercially purchased 4-inch GaAs LED epitaxial wafer. The epitaxial structure is composed by p-GaAs layer, multiple quantum wells (active region) and n-GaAs layer. We first etch the GaAs epitaxial structure down to the n-GaAs layer to expose GaAs by citric acid wet etching. We then deposit the Ti/Pt metallic contact on the p-GaAs layer using the odd-hour evaporator. Following that, Au/Ge/Ni metallic contacts are deposited on the n-GaAs layer using the AJA sputter deposition system. We then etch the GaAs epitaxial structure down to the bulk substrate to outline the micro-LEDs using citric acid wet etching. In the end, the GaAs wafer is annealed in RTA-AG610 for better n-contact.

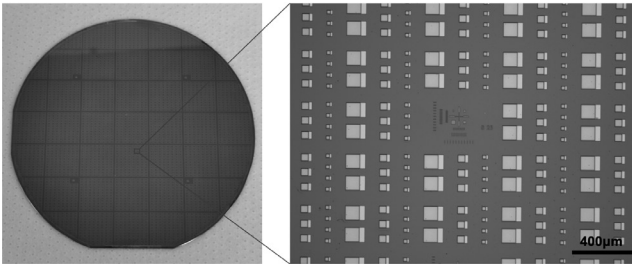


Figure 2: Fabricated GaAs micro-LEDs on a 4-inch GaAs wafer.

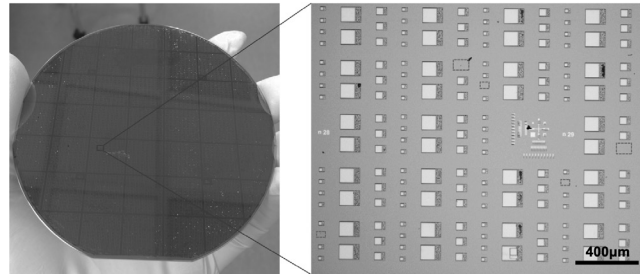


Figure 3: Transferred GaAs micro-LEDs on a 4-inch silicon wafer.

Figure 2 shows micro-LEDs of various sizes.

We then spin-coat PMMA onto the micro-LEDs as the protection layer and bond the 4-inch GaAs wafer with a transparent carrier wafer using a low melting-point thermal plastic polymer. Then we place the stack into citric acid to etch away the bulk GaAs substrate. After that, we have micro-LED arrays attached to the transparent carrier wafer. We then build up an aligning and bonding system based on the ABM contact aligner and a homemade heat stage. Using the aligning and bonding system, we first align the micro-LEDs with the features on the target substrate and then bring the micro-LEDs into contact with the target silicon substrate.

In the end we melt the thermal plastic polymer on a heat stage allowing the removal of the carrier substrate. The polymer residue is etched away in acetone. The result is aligned micro-LEDs transferred onto a 4-inch silicon wafer (Figure 3).

The transfer yield of this method is promising.

We transferred micro-LEDs in varied sizes to a bare silicon substrate (no adhesion layer) with high yield. The dashed boxes in Figure 3 indicate the few missing micro-LEDs, which are a small fraction of the total. The alignment accuracy is quantified by thousands of alignment marks distributed across the wafer. They show our method has reasonably precise alignment ($\sim 1\mu\text{m}$). This wafer-scale transfer method will make possible new classes of integrated wireless sensors and optoelectronic devices fabricated across a full 4-inch wafer.

References:

- [1] Cortese, Alejandro J., et al. "Microscopic sensors using optical wireless integrated circuits." Proceedings of the National Academy of Sciences (2020).

Optomechanical Sensing in the Nonlinear Saturation Limit

CNF Project Number: 1997-11

Principal Investigator(s): Qiang Lin

User(s): Usman A. Javid

Affiliation(s): The Institute of Optics, University of Rochester, Rochester NY

*Primary Source(s) of Research Funding: National Science Foundation
(Grant No. ECCS-1842691, ECCS-1351697, and EFMA-1641099)*

Contact: qiang.lin@rochester.edu, usman.javid@rochester.edu

Primary CNF tools used: JEOL 9500, Unaxis 770 deep silicon etcher

Abstract:

The leap from former bulky electronic and optical components to integrated devices has revolutionized computing, information processing and sensing technologies. Compact chip-scale devices allow confinement of light into sub-wavelength volumes to enable strong light matter interactions. The interaction of light with mechanical motion has enabled design of highly sensitive opto-mechanical sensors that are used in many areas of scientific research. These sensors have a limited dynamic range of sensing in order to allow for high sensitivity of detection. Here, we demonstrate that the dynamic range can be enhanced by a new measurement technique using a suspended silicon microdisk resonator that supports high- Q optical and mechanical modes.

Summary of Research:

Interaction of light with mechanical motion has enabled many interesting phenomena including cooling and mechanical lasing, quantum state control of light and mechanical motion, nonlinear and chaotic dynamics and so on [1]. Light-matter interactions inside optical microcavities have been shown to be excellent sensors [2]. For instance, these devices have been used in force sensing [3], acceleration and gyration measurements [4], electric magnetic fields sensors [5], scanning-probe microscopy [6], chemical and biological sensors [7], and so on. In most sensors there is a trade-off between the sensitivity that determines the smallest change in the input that can be detected, and the dynamic range that determines the largest change in the input that can be transduced without saturation. Cavity based optical sensors rely on the change in the resonance frequency of the cavity mode due to the change in the environment. This is manifested in the change in the transmission of an optical signal through the cavity. The nonlinear nature of the Lorentzian lineshape of the cavity mode puts an upper limit on the maximum change in its resonance frequency that can be measured. Increasing this dynamic range requires increasing the cavity linewidth which decreases the sensitivity to the resonance shift, manifesting the sensitivity-dynamic range trade-off mentioned earlier. Here we demonstrate a technique that extends the dynamic range beyond the traditional limit.

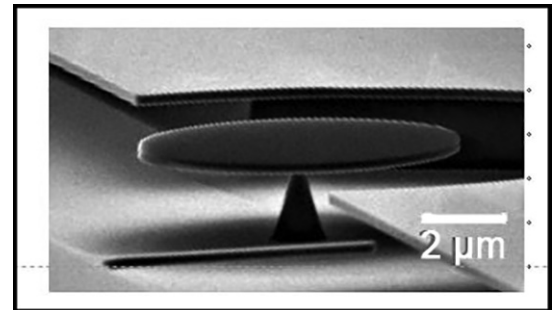


Figure 1: SEM image of the silicon microdisk resonator.

The scanning electron microscopic (SEM) image in Figure 1 shows a high- Q silicon microdisk resonator fabricated from a standard silicon-on-insulator (SOI) wafer using electron-beam lithography (JEOL 9500). The microdisk has a radius of about $4\ \mu\text{m}$ and thickness of $260\ \text{nm}$. A $\text{C}_4\text{F}_8/\text{SF}_6$ chemistry was utilized in an inductively coupled plasma-reactive ion etching (ICP-RIE) process on the Unaxis 770 deep silicon etcher. The recipe was optimized for smooth device sidewalls, which reduces scattering losses and improves the optical quality (Q) of the device. Additionally, a hydrofluoric acid (HF) undercut was employed to suspend the silicon microdisk above the oxide layer.

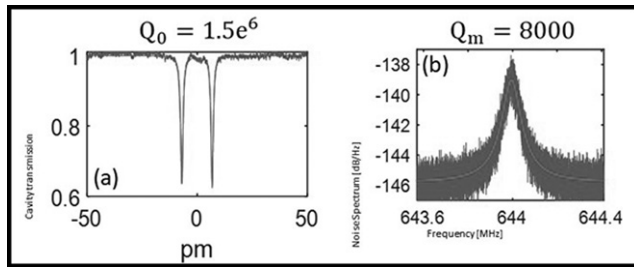


Figure 2: (a) Spectrum of an optical resonance of the microdisk with an intrinsic Q of 1.5 million. (b) Thermal noise spectrum of the mechanical breathing mode with a Q of 8000 measured in vacuum.

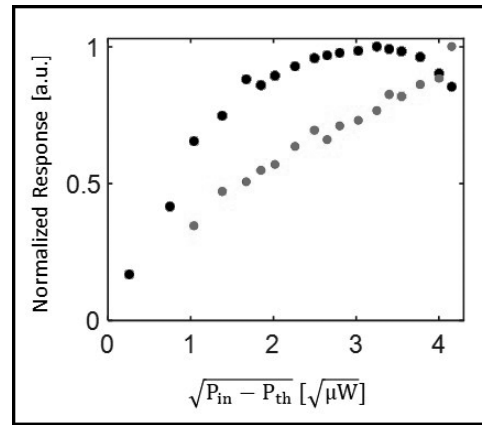


Figure 3: Measured modulation amplitude for increasing pump power using only the first harmonic (black) and the first three harmonics (grey). P_{th} : Lasing threshold power, P_{in} : Input laser power.

This undercut was done in several steps using a dilute HF bath to precisely control the undercut. The pedestal width is estimated to be between 100 and 200 nm. The resonator supports optical modes with quality factor as high as 1.5 million as shown in Figure 2(a). The device also supports a radial breathing mechanical mode with a resonance frequency of 644 MHz and a Q -factor of around 8000 in vacuum as shown in Figure 2(b).

Typically, in a sensing experiment, a modulation signal is applied to the cavity to modulate the resonance frequency in time. In optomechanical systems, this can be done by coherent oscillations induced by radiation pressure [8]. In this case, the cavity starts coherent mechanical oscillations after a power threshold is reached and the mechanical energy increases linearly with the input optical power. Theoretically, the dynamics can be modelled as a harmonic oscillator with time dependent resonance frequency. In the limit where the mechanical resonance frequency exceeds the cavity linewidth, we have shown that the mechanical motion can be estimated unambiguously by the first three harmonics of the modulation [9]. This is a new technique that allows the measurement of modulation amplitudes that exceed the ordinarily achievable dynamic range, given by the cavity linewidth.

We run a pump-probe experiment where a low- Q resonance drives these mechanical oscillations while a high- Q mode acts as a probe to measure the modulation amplitude. We compare the measured modulation amplitude using the traditional method using only the first harmonic, and our proposed approach using the first three harmonics of the modulation signal. Figure 3 shows the results. We can clearly see that the measurement using the traditional approach of using

only the first harmonic saturates while our technique gives a linear response proving an increase of dynamic range. We measure a maximum modulation amplitude of over six times larger than the dynamic range would ordinarily allow.

Conclusions:

We have demonstrated a new sensing technique for micro-resonator based optomechanical sensors. Experimentally, we have shown how our proposed approach can extend the dynamic range of these sensors far beyond what is traditionally achievable.

References:

- [1] M. Aspelmeyer, T. J. Kippenberg, and F. Marquardt, *Rev. Mod. Phys.* 86, 1391 (2014).
- [2] M. R. Foreman, J. D. Swaim, and F. Vollmer, *Adv. Optics Photonics* 7, 168-240 (2015).
- [3] E. Gavartin, P. Verlot, and T. J. Kippenberg, *Nat. nanotechnology* 7, 509 (2012).
- [4] J. Li, M.-G. Suh, and K. Vahala, *Optica* 4, 346-348 (2017).
- [5] S. Forstner, S. Prams, J. Knittel, E. Van Ooijen, J. Swaim, G. Harris, A. Szorkovszky, W. Bowen, and H. Rubinsztein-Dunlop, *Phys Review Letters* 108, 120801 (2012).
- [6] Y. Liu, H. Miao, V. Aksyuk, and K. Srinivasan, *Opt. Express* 20, 18268-18280 (2012).
- [7] Y. Sun and X. Fan, *Anal. Bioanalytical Chemistry* 399, 205-211 (2011).
- [8] H. Rokhsari, T. J. Kippenberg, T. Carmon, and K. J. Vahala, *Opt. Express* 13, 5293-5301 (2005).
- [9] U. Javid, et al., *Conference on Lasers and Electro-Optics (CLEO) 2020*. (In preparation).

Photon-Level Tuning of Photonic Nanocavities

CNF Project Number: 1997-11

Principal Investigator(s): Qiang Lin

User(s): Mingxiao Li, Yang He, Jingwei Ling

Affiliation(s): Electrical and Computer Engineering, University of Rochester

Primary Source(s) of Research Funding: National Science Foundation (NSF) (EFMA-1641099, ECCS-1810169, and ECCS-1842691); the Defense Threat Reduction Agency-Joint Science and Technology Office for Chemical and Biological Defense (grant No. HDTRA11810047)

Contact: qiang.lin@rochester.edu, mli53@ur.rochester.edu, yhe26@ur.rochester.edu, jling8@ur.rochester.edu

Primary CNF Tools Used: JEOL 9500, AJA ion mill

Abstract:

We report an all-optical approach for extremely efficient tuning of a high- Q lithium niobate photonic crystal nanocavity, with a significant resonance tuning rate of 88.4 MHz/photon.

Summary of Research:

Controlling photonic functionalities by purely optical means is a long-term goal of nonlinear optics, which has been pursued for decades. Unfortunately, natural optical media generally exhibit fairly weak optical nonlinearities. Photonic crystal (PhC) nanocavities are able to strongly confine optical waves inside a small volume, thus particularly suitable for enhancing nonlinear optical interactions [1]. To date, PhC nanocavities have been applied on a variety of device platforms for optically tuning/switching the cavity properties [2-6]. However, it remains fairly challenging to achieve device control with only photon-level optical energy, which represents the ultimate efficiency of nonlinear optics. Here we report a lithium niobate (LN) PhC nanocavity that exhibits an optical Q as high as 1.41 million, more than one order of magnitude higher than previously reported [7-9]. With this device, we are able to demonstrate extremely efficient wavelength tuning of the device, with a resonance tuning rate as high as 88.4 MHz/photon, and nearly 100% preservation of the resonance quality.

Figure 1 shows the device, which was fabricated on a 300-nm-thick x-cut single-crystalline LN thin film, and patterned by JEOL 9500. We optimized the nanobeam width, layer thickness, lattice constant, and the shape

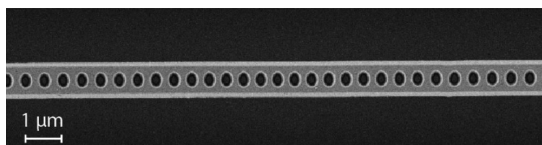


Figure 1: SEM image of a fabricated LN PhC nanobeam.

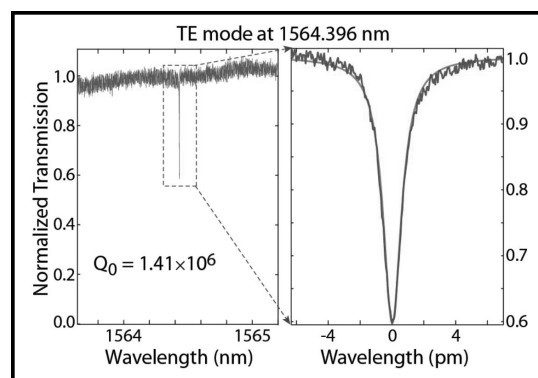


Figure 2: Laser-scanned transmission spectrum of a fabricated LN PhC nanobeam with the experimental data shown in blue and the theoretical fitting shown in red. (See pages vi-vii for full color version.)

of the elliptical holes to achieve a photonic bandgap of 26 THz covering optical frequency from 183 to 209 THz, for the transverse-electric-like (TE-like) polarization with the guided mode dominantly lying in the device plane. Simulations by the finite element method show that the cavity mode exhibits a radiation-limited optical Q of 1.23×10^8 , with an effective mode volume as small as $0.78(\lambda/n)^3$.

Detailed experimental characterization of the fabricated device, as shown in Figure 2, shows that the device exhibits a high-quality cavity mode at 1564.396 nm in the telecom band, with an intrinsic optical Q factor as high as 1.41 million. This value is more than an order of magnitude larger than what was previously reported on LN nanophotonic devices [7-9]. To the best of our

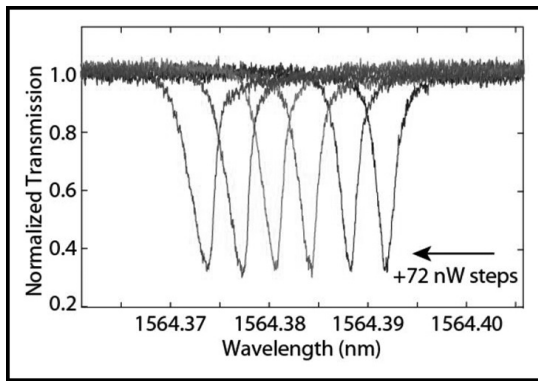


Figure 3: Measured transmission spectra of cavity exhibit strong resonant wavelength tuning with increasing intra-cavity power. (See pages vi-vii for full color version.)

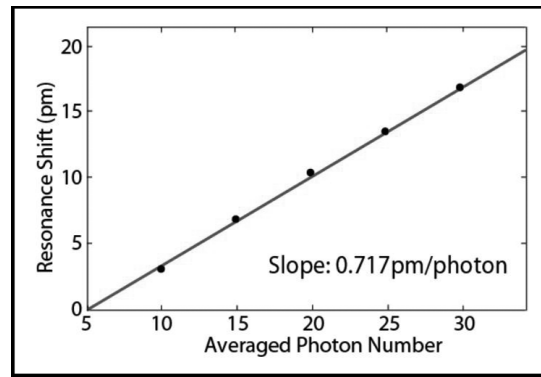


Figure 4: Linear resonant wavelength tuning as a function of intra-cavity power. The measured tuning efficiency is 88.4 MHz/photon, or equivalently 0.67 GHz/aJ.

knowledge, this is the second single-crystalline PhC nanocavity, other than silicon ones [10], that is able to exhibit an intrinsic optical Q above one million.

The extremely high optical Q , together with the tiny effective mode volume, of the device would result in dramatic enhancement of nonlinear optical interactions inside the cavity, thus allowing us to explore efficient nonlinear photonic functionalities. An intriguing nonlinear optical property of LN is the photorefractive effect [11], which manifests an intensity-dependent decrease of refractive index. We thus expect that the cavity resonance can be self-tuned by optical power launched into the device. To show this phenomenon, we maintain an external coupling efficiency of 65% (accordingly, loaded optical Q around 8.9×10^5). We continuously scanned the laser wavelength across the resonant wavelength back and forth and monitored the transmission of the device. As shown in Figure 3, when the input optical power increases from 72 nW to 432 nW, the cavity resonance wavelength continuously shifts towards blue.

As the laser wavelength was scanned back and forth in a periodic triangular fashion over a spectral range of 150 pm, the input power of 432 nW results in an averaged optical energy of about 3.96 aJ inside the cavity, which corresponds to an average of only 30 photons. Figure 4 shows the induced resonance shift as a function of average number of photons inside the cavity. It shows a clear linear dependence, with a tuning slope of 0.717 pm/photon, corresponding to 88.4 MHz/photon. Therefore, about 2.4 photons on average inside the cavity are able to shift the whole cavity resonance, clearly showing the extreme efficiency of the induced resonance tuning.

In summary, we demonstrated a LN photonic crystal nanobeam resonator with optical Q as high as 1.41 million. With this device, we were able to demonstrate efficient tuning of the cavity resonance, with a significant tuning rate of 88.4 MHz/photon and nearly 100% preservation of the resonance quality.

References:

- [1] M. Soljacic and J. D. Joannopoulos, "Enhancement of nonlinear effects using photonic crystals," *Nature Mat.* 3, 211 (2004).
- [2] M. Notomi, et al., "Nonlinear and adiabatic control of high- Q photonic crystal nanocavities," *Opt. Express* 15, 17458 (2007).
- [3] I. Fushman, et al., "Ultrafast nonlinear optical tuning of photonic crystal cavities," *Appl. Phys. Lett.* 90, 091118 (2007).
- [4] C. Husko, et al., "Ultrafast all-optical modulation in GaAs photonic crystal cavities," *Appl. Phys. Lett.* 94, 021111 (2009).
- [5] K. Nozaki, et al., "Sub-femtojoule all-optical switching using a photonic-crystal nanocavity," *Nature Photon.* 4, 477 (2010).
- [6] K. Nozaki, et al., "Ultralow-power all-optical RAM based on nanocavities," *Nature Photon.* 6, 248 (2012).
- [7] S. Diziain, et al., "Second harmonic generation in free-standing lithium niobate photonic crystal L3 cavity," *Appl. Phys. Lett.* 103, 051117 (2013).
- [8] L. Cai, et al., "Photonic crystal slab fabricated on the platform of lithium niobate-on-insulator," *Opt. Lett.* 39, 2094 (2014).
- [9] H. Liang, et al., "High-quality lithium niobate photonic crystal nanocavities," *Optica* 4, 1251 (2017).
- [10] T. Asano, et al., "Photonic crystal nanocavity with a Q factor exceeding eleven million," *Opt. Express* 25, 1769-1777 (2017).
- [11] P. Günter and J. P. Huignard, eds., *Photorefractive Materials and Their Applications* (Springer, New York, 2006).

Ultra-Low Threshold Broadband Soliton Frequency Comb Generation

CNF Project Number: 2364-15

Principal Investigator(s): Michal Lipson¹

User(s): Xingchen Ji²

*Affiliation(s): 1. Department of Electrical Engineering, Columbia University, New York, NY 10027;
2. School of Electrical and Computer Engineering, Cornell University, Ithaca, NY 14853*

Primary Source(s) of Research Funding: Defense Advanced Research Projects Agency

Contact: ml3745@columbia.edu, xj53@cornell.edu

*Primary CNF Tools Used: PECVD, e-beam lithography, Oxford 100 etcher,
AJA sputter deposition, mask writer, furnace, Oxford 82 etcher*

Abstract:

We measure a record-low threshold power down to 73 μW for parametric oscillation using resonators with intrinsic Q of 31.8 ± 4.4 million and demonstrate a broadband single soliton comb spectrum spanning 1097 nm-2040 nm (126 THz). The resonator compact profile is designed to minimize higher order modes excitation.

Summary of Research:

Microresonator-based frequency comb generation has recently attracted interest due to potential applications in spectroscopy, precision metrology and biomedical imaging [1-8]. However, the thresholds for these broadband frequency combs are limited by loss due to surface scattering [9,10].

Here we demonstrate an ultra-low threshold broadband single soliton frequency comb. It is generated with a resonator based on highly multimode Si_3N_4 waveguides for decreasing loss due to surface scattering and adiabatic bends to suppress higher order modes excitation.

Figure 1(a) shows the schematic of the device. The microresonator has a free spectral range (FSR) of 174 GHz and a cross section of 730 nm \times 2600 nm which supports more than 8 modes (Transverse electric (TE) modes are shown in Figure 1 inset). A bus waveguide with the same dimension is used to couple to it. In the coupling section, the bending radius starts large ($\sim 900 \mu\text{m}$) and then gradually reduces to a small value ($\sim 80 \mu\text{m}$). The bending radius changes adiabatically, which allows us to have a small bending radius and also suppress excitation of higher order modes. Full 3D finite-difference time-domain (FDTD) simulations (Lumerical FDTD) depicted in Figure 2 show that higher order modes in our adiabatic bends design are suppressed compared with a regular ring resonator with constant bending radius.

We achieve a broadband single soliton comb spectrum spanning 1097 nm-2040 nm (126 THz) and measure a record-low threshold power down to 73 μW for parametric oscillation using resonators with intrinsic

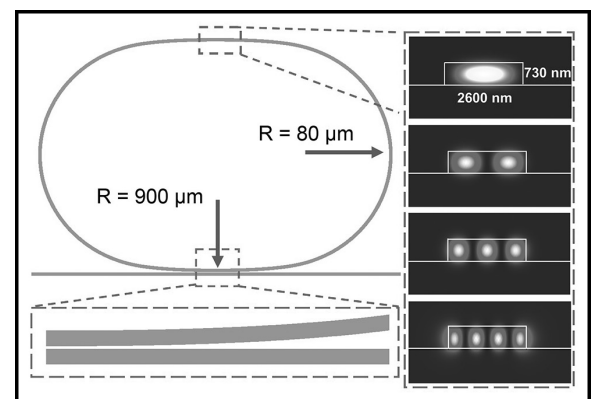


Figure 1: Schematic of our microresonators with adiabatic bends design. The bending radius starts large ($\sim 900 \mu\text{m}$) and then gradually reduces to a small value ($\sim 80 \mu\text{m}$). Inset shows the transverse electric (TE) modes supported by the waveguide and only the fundamental mode is excited in the adiabatic bends design.

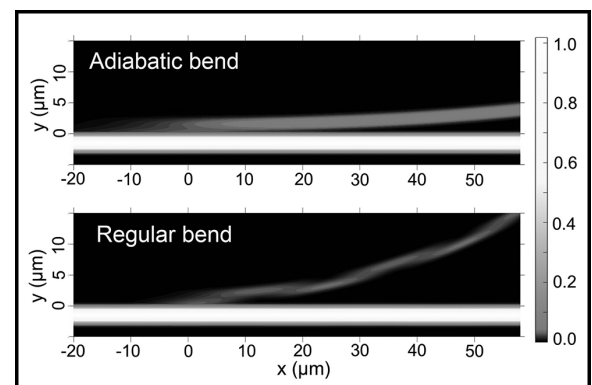


Figure 2: FDTD simulations of the adiabatic bends design (top) and the regular ring resonator with constant bending radius (bottom). Note that higher order modes have been excited in the regular ring and not in our adiabatic bends design.

Q of 31.8 ± 4.4 million. One can see that despite the large waveguide dimensions, we can still engineer the dispersion. In order to test the devices, we launch a laser source transmitted through a fiber polarization controller into the inverse nanotaper of our chip using a lensed fiber and collect the output through another inverse nanotaper using a collimating lens. We then split the collected light such that one of the outputs is used to monitor the generated comb spectrum and the other one is sent to a fast photodiode (> 12.5 GHz) to monitor transmission. We measure the output power in the first generated four-wave-mixing sidebands for different pump powers to determine the threshold for parametric oscillation.

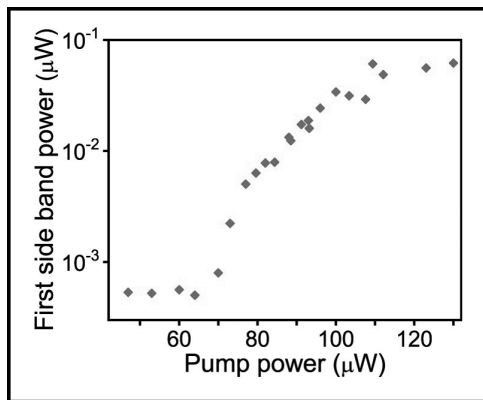


Figure 3: Output power in the first generated side band as a function of pump power. In this device, parametric oscillation is observed for pump power down to 73 μ W.

Figure 3 shows the data for a device with an intrinsic Q of 32.8 million pumped at the resonance near 1560 nm. Parametric oscillation is observed with pump power down to 73 μ W which is close to the theoretical limit of 70 μ W. We generate a soliton-mode locked comb with the thermal tuning method as demonstrated in [11]. A narrow wavelength division multiplexing (WDM) filter centered at the pump wavelength is used to increase the dynamic range of the optical spectrum analyzer (OSA). Limited by the wavelength range of a single OSA, we obtain the spectrum in two shots under the same experimental condition (shown in Figure 4). Soliton state is maintained the same throughout the experiment.

In conclusion, we measure a record-low threshold power down to 73 μ W for parametric oscillation using resonators with intrinsic Q of 31.8 ± 4.4 million.

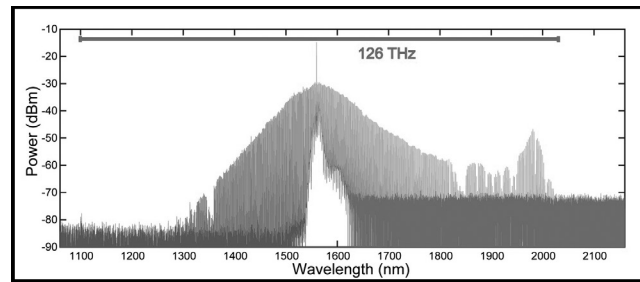


Figure 4: Broadband single soliton frequency comb spanning 1097 nm-2040 nm (126 THz) using highly multimode microresonators. Note that blue and red parts are the same single soliton state measured by two OSAs and dips in the spectrum (at 1350 nm and 1850 nm for example) are due to the WDM filter defects.

We achieve a broadband single soliton comb spectrum spanning 1097 nm-2040 nm (126 THz) using highly multimode waveguides by suppressing excitation of higher order modes with adiabatic bends. Utilizing highly multimode structures, we have more flexibility in the waveguide design (i.e. dispersion engineering). This work provides a method for using ultra high- Q multimode microresonators for applications such as spectroscopy and precision metrology.

References:

- [1] T. J. Kippenberg, A. L. Gaeta, M. Lipson, and M. L. Gorodetsky, *Science* 361, eaan8083 (2018).
- [2] A. L. Gaeta, M. Lipson, and T. J. Kippenberg, *Nat. Photonics* 13, 158-169 (2019).
- [3] M.-G. Suh, Q.-F. Yang, K. Y. Yang, X. Yi, and K. J. Vahala, *Science* 354, 600-603 (2016).
- [4] A. Dutt, C. Joshi, X. Ji, J. Cardenas, Y. Okawachi, K. Luke, A. L. Gaeta, and M. Lipson, *Sci. Adv.* 4, e1701858 (2018).
- [5] X. Ji, X. Yao, A. Klenner, Y. Gan, A. L. Gaeta, C. P. Hendon, and M. Lipson, *Opt. Express* 27, 19896-19905 (2019).
- [6] M. H. P. Pfeiffer, C. Herkommer, J. Liu, H. Guo, M. Karpov, E. Lucas, M. Zervas, and T. J. Kippenberg, *Optica* 4, 684-691 (2017).
- [7] M. Karpov, M. H. Pfeiffer, J. Liu, A. Lukashchuk, and T. J. Kippenberg, *Nat. Commun.* 9, 1146 (2018).
- [8] Q. Li, T. C. Briles, D. A. Westly, T. E. Drake, J. R. Stone, R. B. Ilic, S. A. Diddams, S. B. Papp, and K. Srinivasan, *Optica* 4, 193-203 (2017).
- [9] X. Ji, A. B. Felipe, S. P. Roberts, A. Dutt, J. Cardenas, Y. Okawachi, A. Bryant, A. L. Gaeta, and M. Lipson, *Optica* 4(6), 619 (2017).
- [10] M. H. P. Pfeiffer, J. Liu, A. S. Raja, T. Morais, B. Ghadiani, and T. J. Kippenberg, *Optica* 5(7), 884 (2018).
- [11] C. Joshi, J. K. Jang, K. Luke, X. Ji, S. A. Miller, A. Klenner, Y. Okawachi, M. Lipson, and A. L. Gaeta, *Opt. Lett.* 41, 2565 (2016).

Development of Single and Double Layer Anti-Reflective Coatings for Astronomical Instruments

CNF Project Number: 2458-16

Principal Investigator(s): Gordon Stacey¹

User(s): Bugao Zou², Nicholas Cothard², Mahiro Abe³

Affiliation(s): 1. Department of Astronomy, 2. Department of Applied and Engineering Physics, 3. Department of Physics; Cornell University

Primary Source(s) of Research Funding: NASA Grant NNX16AC72G

Contact: stacey@cornell.edu, bz332@cornell.edu, nc467@cornell.edu, ma797@cornell.edu

Primary CNF Tools Used: Oxford PECVD, Anatech resist strip, Oxford 82 & 100 etchers, manual resist spinners, resist hot strip bath, Plasma-Therm deep silicon etcher, ASML 300C DUV stepper

Abstract:

We are developing microfabricated, silicon-substrate based mirrors for use in cryogenic Fabry-Perot Interferometers (FPIs) for astronomical instruments in the mid-infrared to sub-mm/mm wavelength regime. These mirrors consist of silicon substrates that are lithographically patterned with metal mesh reflectors on one side and metamaterial anti-reflection coatings (ARC) on the other side. In the past year we published a paper in the *Journal of Low Temperature Physics* that illustrates the design of the CCAT-prime Epoch of Reionization Spectrometer instrument and how the microfabricated FPI fits in the module and enables our scientific goals. Currently we are refining our ARC fabrication recipe to improve the quality and accuracy of the microfabricated structures. Optical performance measurements for our samples are ongoing using Fourier transform spectrometers.

Summary of Research:

The goal of the project is to develop microfabricated, silicon-substrate based mirrors for use in cryogenic Fabry-Perot interferometers for astronomical instruments in the mid-infrared to sub-mm/mm wavelength regimes. The mirrors consist of high-purity, float-zone, 500- μm -thick silicon wafers that are lithographically patterned with frequency-selective, gold mesh reflectors. We use a combination of inductive and capacitive meshes to maintain uniform high reflectance and hence nearly uniform resolving power over the FPI bandwidth. Due to the high index of refraction of silicon, the other side of the mirror must be patterned with an ARC to achieve broadband capability and to mitigate contaminating resonances from the silicon surface [1,2].

The bulk of our work this year has been the development of the fabrication methods of the ARC. Figure 1 shows our current recipe for a two-layer ARC. First, silicon dioxide is deposited on the wafer using the Oxford plasma enhanced chemical vapor deposition (PECVD) tool. Then, two layers of photoresist are patterned correspondingly to be etched into a two-layer oxide pattern using the Oxford 100 etcher. We use either the ABM contact aligner or the ASML stepper to pattern the photoresist depending on the feature sizes of our structures. After that, the two-layer silicon structure is formed by etching the wafer using the Plasma-Therm

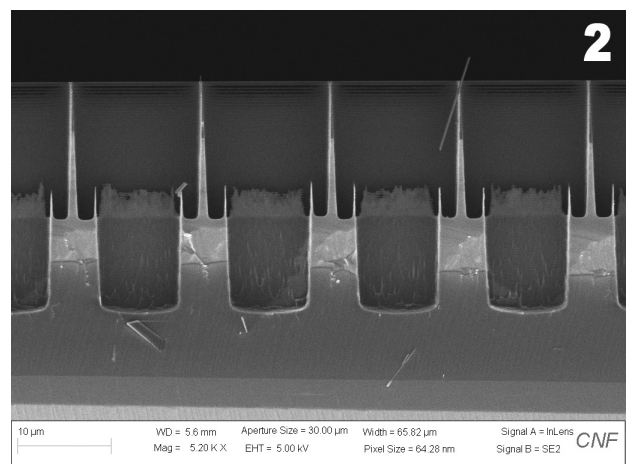
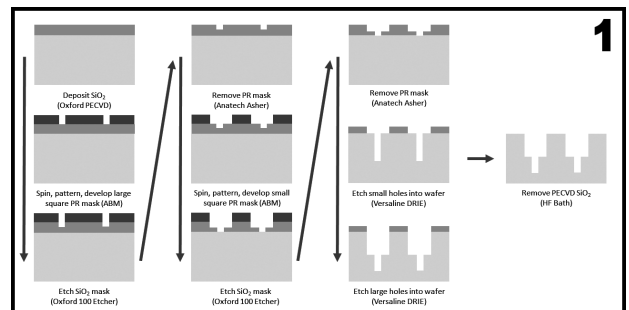


Figure 1, top: Process flow for fabricating a double-layer ARC on a silicon wafer. **Figure 2, bottom:** SEM image taken using CNF's Zeiss Ultra SEM showing the two-layer structure of anti-reflection coatings.

deep silicon etcher using the oxide layer as the etch mask. A scanning electron microscope (SEM) image of the cross section of the ARC is shown in Figure 2.

Unwanted fence-like structures can be found at the boundary of two silicon layers. We believe they are caused by the passivation layer generated during silicon etch processes. We found that an external thermal oxidation postprocessing step can remove these structures. We are currently working to improve our control of this method and we are also looking for other methods to prevent the formation of this structure.

In addition, our fabrication process for metal mesh reflectors has been improved over this past year. We have successfully deposited 10-micron scale capacitive and inductive gold meshes on samples using AZ nLOF 2020 photoresist and the CHA evaporator. The lift-off procedure is done using heated Microposit 1165 Remover.

We have fabricated both ARC and metal mesh reflectors on several optical quality silicon wafers and are now measuring their frequency dependent transmittances in the mid-infrared to sub-mm/mm wavelength regimes using Fourier transform spectrometers. Our progress on these devices is discussed in a paper published in *Journal of Low Temperature Physics* which illustrates the design of the CCAT-prime Epoch of Reionization Spectrometer instrument and how the microfabricated FPI fits in the module and enables spectroscopic observations of the early universe [1].

The silicon-substrate based mirrors that are developed in CNF will be used in the upcoming scanning FPI instrument Prime-Cam in the CCAT-prime observatory, which is located at 5600 meters elevation on Cerro Chajnantor in the Atacama Desert in Chile [3]. CCAT-

prime will use our FPI for one of its main science goals, that is to study the Epoch of Reionization of the universe via [CII] intensity mapping in the 750-1500 μm regime. Our instrument will enable the intensity mapping observations by providing high-sensitivity, wide-field, broadband spectroscopy. These measurements will tell us about how the first stars and galaxies evolved in the early universe.

Conclusions and Future Steps:

In the past year we have made great steps towards achieving our goals at CNF. We have demonstrated our ability to fabricate double-layer ARCs for different wavelengths and metal meshes with different feature sizes. We have used many of the fabrication and metrology tools at CNF. Our next steps are to better characterize our etched geometries and improve our metamaterial ARCs. We will be using Fourier transform spectrometers to measure our samples optical performance and using the results to iterate on our fabrication design.

References:

- [1] Cothard, N.F., Choi, S.K., Duell, C.J., et al. The Design of the CCAT-prime Epoch of Reionization Spectrometer Instrument. *J Low Temp Phys*, <https://doi.org/10.1007/s10909-019-02297-1> (2020).
- [2] N.F. Cothard, M. Abe, T. Nikola, G.J. Stacey, G. Cortes-Medellin, P.A. Gallardo, B.J. Koopman, M.D. Niemack, S.C. Parshley, E.M. Vavagiakis, K. Vetter, "Optimizing the efficiency of Fabry-Perot interferometers with silicon-substrate mirrors," *Advances in Optical and Mechanical Technologies for Telescopes and Instrumentation III* (2018).
- [3] <http://www.ccatobservatory.org/>

Fabrication, Characterization, and Application of All-Glass, 1 cm Diameter Metalens Working at Visible Wavelength

CNF Project Number: 2471-16

Principal Investigator(s): Professor Federico Capasso

User(s): Joon-Suh Park

Affiliation(s): John A. Paulson School of Engineering and Applied Sciences, Harvard University

Primary Source(s) of Research Funding: Defense Advanced Research Projects Agency (Grant no. HR00111810001)

Contact: capasso@seas.harvard.edu, parkj@g.harvard.edu

Website: <https://www.seas.harvard.edu/capasso>

Primary CNF Tools Used: Heidelberg DWL2000, HamaTech mask chrome etch 1, ASML 300C DUV stepper, Gamma automatic coat-develop tool, CHA Mark 50 e-beam evaporator, Trion Minilock III ICP etcher, Plasma-Therm dual chamber 770, Oxford 81, Oxford 82, Oxford 100, P10 profilometer, DISCO dicing saw, Zeiss Ultra SEM

Abstract:

Using deep-ultraviolet (DUV) projection lithography, we demonstrate mass-production of one-centimeter diameter, all-glass metalenses working in the visible wavelength. Characterization of the metalens by comparing its point-spread-function with that of the ideal lens and conventional refractive lenses with similar size and focal lengths are performed.

Summary of Research:

Recent advances in aerial drones and cube satellites have increased the demands for better optics for their on-board imaging systems. One of the approaches for better imaging is increasing the amount of light collected into the system by increasing the diameter of the lens. However, increasing the diameter of the lens meets two important tradeoffs for their application purposes: the increase of aberration and the weight of the lens. Simply increasing the diameter of a refractive lens increases the spherical aberration, which then needs to be corrected by using costly methods such as tailoring the lens surface to an aspheric. Also, the weight of the bulk refractive optics volumetrically scales with diameter, which renders it less advantageous when payload is of a concern.

Metasurfaces, a new category of optical elements that can tailor the optical effects of the outgoing light by placing subwavelength-spaced structures on a two-dimensional surface, can provide alternative solutions for refractive optics [1]. Although many prior metasurface works used high-refractive index materials such as TiO_2 , SiN, GaN or amorphous Si to achieve phase control [1,2], here we use low-refractive index material, fused silica (SiO_2), as a base material to design and fabricate a centimeter diameter metasurface functioning as a lens (metalens) working in the visible wavelength.

We fabricate the metalenses on a 4-inch fused silica wafer using DUV (248 nm, KrF) projection lithography. After writing a reticle of the metalens with Heidelberg DWL 2000 mask writer, the pattern on the reticle is exposed onto the chrome (100 nm thick)-coated fused

silica substrate spin-coated with DUV-24P ARC and UV210 resist. The patterned resist is then used as an etch mask to transfer the pattern to the chrome layer using chlorine plasma. As chlorine etch chemistry has high selectivity against SiO_2 , the substrate works as an etch stop layer. With the patterned chrome as etch mask, we then etch into the SiO_2 substrate using fluorine plasma. The fluorine etch chemistry has high selectivity between chrome and SiO_2 , which allows high-aspect ratio etching of SiO_2 . The fluorine etching is stopped when the etch depth reaches 2 μm , which is determined by surface profilometry. The residual chrome is then etched away using chlorine plasma, leaving only SiO_2 pillars on the substrate. The schematic of the process is depicted in Figure 1, and the scanning electron microscope imaging result of fabricated SiO_2 pillars is shown in Figure 2.

The fabricated metalens is capable of imaging in the visible wavelength, as shown in Figure 3. We further compare the metalens' point-spread-function along its optic axis at metalens' design wavelength ($\lambda = 633 \text{ nm}$) with similar off-the-shelf refractive lens counterparts with similar diameter and focal length; an aspheric lens (Edmund Optics, 33-944) and a plano-convex lens (Thorlabs Inc., LA1213-A). As shown in Figure 4, the fabricated metalens show good focusing around its focus compared to that of the refractive optics. The Strehl ratio of the metalens' focal spot is measured to be 0.95, which indicates the fabricated metalens is diffraction-limited. The results are published to Nano Letters [3].

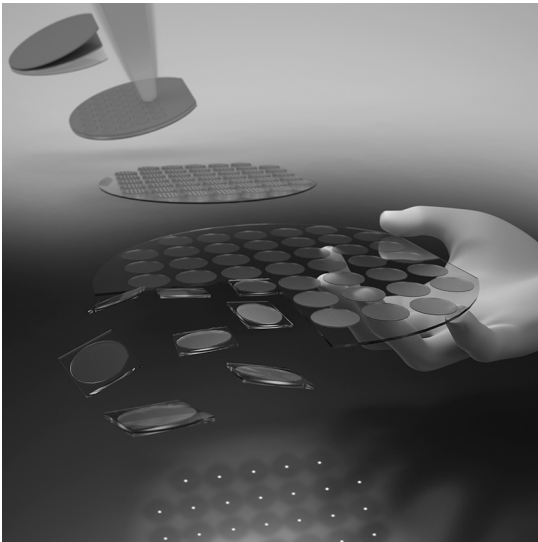


Figure 1: Schematic of fabrication process. A 4-inch diameter fused silica wafer goes through metal evaporation, DUV projection lithography, etching, and dicing to make 45 1-centimeter diameter metalenses per wafer.

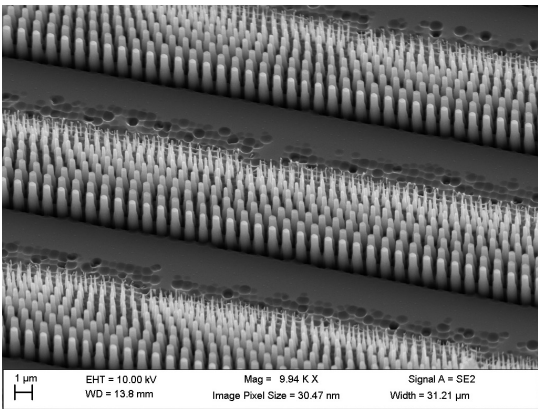


Figure 2: SEM image of silica nanopillars constituting the fabricated metalenses.

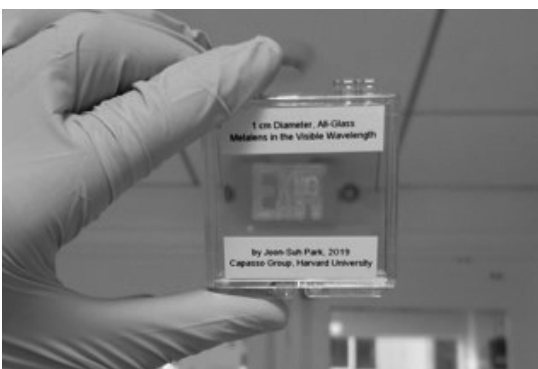


Figure 3: Photograph of a metalens, diced to a 11 mm x 11 mm square from initially fabricated 4-inch wafer, imaging a red-lit emergency exit sign. The image of the "Exit" sign is clearly visible through the metalens.

Conclusions and Future Steps:

We demonstrated a proof-of-concept mass-manufacturing of centimeter-scale metalenses working in the visible wavelength and showed that it does not experience spherical aberrations as its refractive counterparts. However, our metalens is chromatic by design: the focal length varies with incident wavelength. We are investigating methods to design and fabricate a larger diameter metalens and an achromatic metalens that is compatible with conventional integrated circuit chip fabrication techniques.

References:

- [1] Alan She, Shuyan Zhang, Samuel Shian, David R. Clarke, and Federico Capasso, "Large area metalenses: design, characterization, and mass manufacturing," *Opt. Express* 26, 1573-1585 (2018).
- [2] Mohammadreza Khorasaninejad, Wei Ting Chen, Robert C. Devlin, Jaewon Oh, Alexander Y. Zhu, and Federico Capasso, "Metalenses at visible wavelengths: Diffraction-limited focusing and subwavelength resolution imaging," *Science* 352, 1190 (2016).
- [3] Joon-Suh Park, Shuyan Zhang, Alan She, Wei Ting Chen, Peng Lin, Kerolos M. A. Yousef, Ji-Xin Cheng, and Federico Capasso, "All-Glass, Large Metalens at Visible Wavelength Using Deep-Ultraviolet Projection Lithography," *Nano Lett.* 19, 12, 8673-8682 (2019).

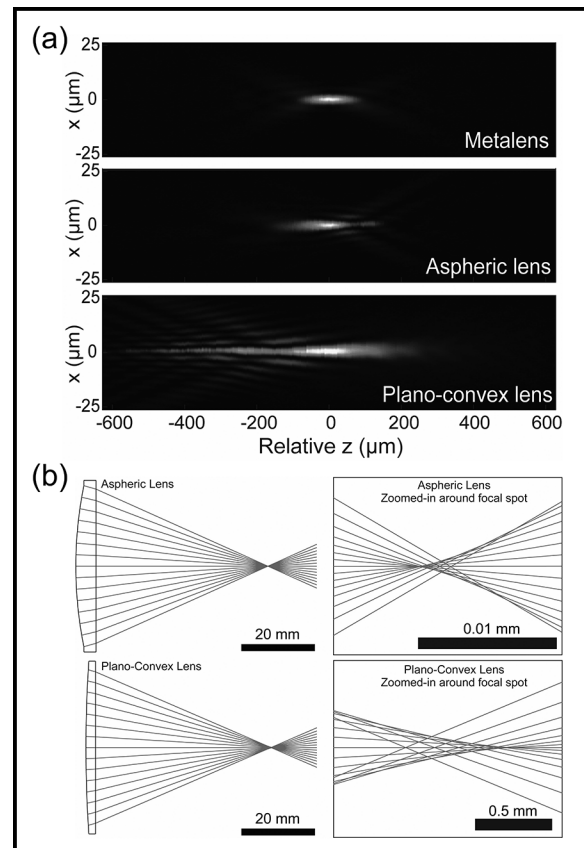


Figure 4: (a) Comparison of point-spread-functions along the optical axis near the focus between a metalens, an aspheric lens (Edmund Optics, 33-944), and a plano-convex lens (Thorlabs Inc., LA1213-A), respectively, with 633 nm wavelength incidence. The refractive lenses are off-the-shelf commercial glass lenses with similar diameter and focal length with those of the metalens. (b) Ray-tracing diagram of refractive lenses derived from data provided by manufacturers.

Tunable Semiconductor Metasurfaces for Active Lensing

CNF Project Number: 2472-16

Principal Investigator(s): Gennady Shvets

User(s): Melissa Bosch, Steven He Huang, Maxim Radikovich Shcherbakov

Affiliation(s): School of Applied and Engineering Physics, Department of Physics; Cornell University

Primary Source(s) of Research Funding: Office of Naval Research (ONR) and National Science Foundation (NSF)

Contact: gs656@cornell.edu, mb2583@cornell.edu, hh623@cornell.edu, mrs356@cornell.edu

Website: <http://shvets.aep.cornell.edu>

Primary CNF Tools Used: JEOL 9500, Zeiss Ultra SEM, Oxford Cobra ICP etcher, Oxford PECVD

Abstract:

Optically thin metamaterials, or metasurfaces, provide strong modulations to spatial and spectral properties of light. We engineer metasurfaces based on high index low-loss semiconductors, which exhibit narrowband and/or tunable optical resonances for near-infrared photonic applications. We report on the design, fabrication, and characterization of resonant silicon metasurfaces and thermally-tunable germanium metasurfaces to demonstrate active lensing. By virtue of their scalability and compactness, semiconductor metasurfaces present a promising alternative to traditional optical elements.

Summary of Research:

Silicon Metasurfaces. Semiconductor resonators, such as germanium and silicon, are attractive candidates for efficient metadevices owing to their high refractive index, infrared transparency, and support of strong localized Mie-type resonance modes [1,2].

Our project focuses on the design and fabrication of resonant amorphous silicon (α -Si) meta-surfaces with sub-50 nm feature sizes, suitable for various applications where compact and efficient light modulation is needed. An example of a typical α -Si metasurface under study is shown in Figure 1, consisting of an array of rectangular α -Si patches on a fused silica substrate, with the gap between adjacent resonators governing the Q -factor of the optical resonance.

In one application, we employ α -Si metasurfaces towards the design and fabrication of a metalens with tunable focus. Metalenses with tunable functionalities are critical to the miniaturization of vision and imaging technologies such as spatial light modulators and adaptive optics; however, most metalenses have static functionalities preset by their geometries. By selecting three constituent resonator geometries that impart phase shifts in increments of $2\pi/3$, the spatial phase profile for a converging metalens is achieved. To enable tunability, the meta-atoms are designed to have a locally-adjustable optical phase response dependent on

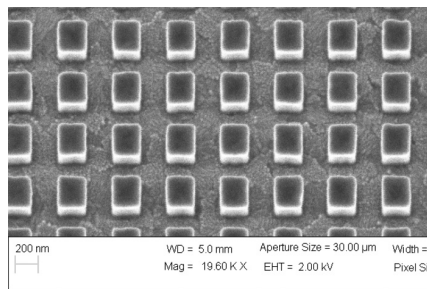


Figure 1: SEM of a typical α -Si-based near-IR resonant metasurface on a SiO_2 /ITO substrate.

the permittivity of the surrounding media, and the lens is encapsulated in a liquid crystal (LC) cell, which offers an absolute shift up to 0.7 in the in-plane permittivity upon application of an external electric field.

For metasurface fabrication, amorphous silicon (α -Si) films are deposited onto ITO-covered fused silica substrates using plasma-enhanced chemical vapor deposition (Oxford PECVD), and film surface

is treated with SurPass 3000 adhesion promoter. HSQ 6% was spun and baked to form a 100 nm thick layer over the α -Si, coated with DisCharge anti-charging layer, e-beam exposed at a dose of $250 \mu\text{C}/\text{cm}^2$ (JEOL 9500FS), and developed in MIF 300 solution for 120 s. The pattern was transferred to the α -Si layer using reactive ion etch (Oxford Cobra). The resulting samples were characterized with a scanning electron microscope (Zeiss Ultra). The project is currently in the LC encapsulation stage. Our simulations predict a focal spot position shift from +8 mm to -8 mm in response to the maximum permittivity modulation of the LC, as shown in Figure 2.

Germanium Metasurfaces. Next, we utilize the large thermo-optic coefficient of germanium (Ge) [3] to demonstrate a resonant Ge-based metalens, which can be controlled by heat. The metalens building blocks are high aspect-ratio anisotropic double-pillar Ge meta-

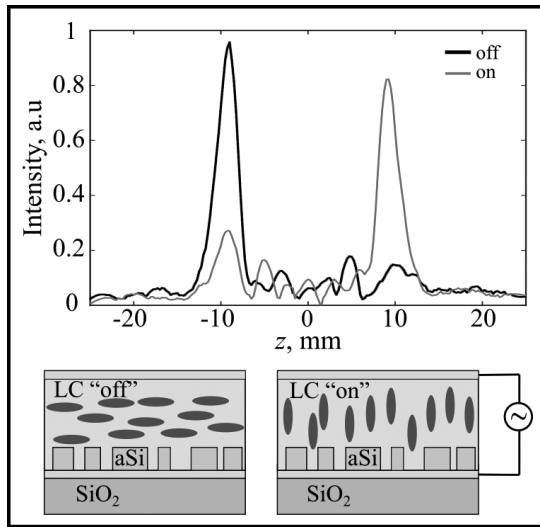


Figure 2: Top, simulated intensity of light transmitted through the α -Si metalens, plotted along the optical axis of the lens. The lens acts as a converging lens with +8 mm focus in the absence of an external electric field (black line) and acts as a diverging lens with a -8 mm focus in the presence of an external electric field (light gray line). Bottom, schematic of an α -Si metalens design.

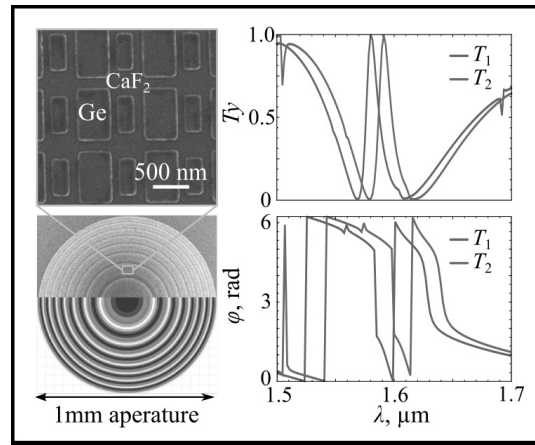


Figure 3: Top Left, zoomed-in SEM of one of the fabricated metalens phase steps. Bottom Left, an SEM of the fabricated 8-step spherical metalens. The lower half of the lens is color-coded according to its eight phase steps. Right, simulated temperature-dependent transmission and phase spectra for one of the meta-atom geometries (zone 8).

atoms, as shown in Figure 3. Such structures support high quality-factor resonances which can be excited by one of the principal linear polarizations of an incident light and whose spectral positions can be widely tuned by heating the metasurface [4]. The meta-atom geometries are selected to impart the required hyperbolic phase profile for a spherical lens, while simultaneously optimized to exhibit high efficiency contrast with thermal tuning. The selection therefore enables control over the intensity of the focused light. Representative transmission and phase spectra of the meta-atoms are presented in Figure 2. We verify the tunable metalens concept experimentally by fabricating and characterizing a Ge metasurface patterned on a quartz substrate. The device fabrication consisted of seven steps: e-beam evaporation of 630 nm of Ge (CVC SC4500); standard PMMA spin-coat, baking, and e-beam exposure at 1000 $\mu\text{C}/\text{cm}^2$ (JEOL 9500FS); development in MIBK:IPA 1:3; e-beam evaporation of a 30 nm chrome (Cr) mask; liftoff in room-temperature sonicated acetone for 20 min; pattern transfer to the Ge layer through HBr reactive ion etching (Oxford Cobra); and removal of residual Cr mask with argon ion milling (AJA Ion Mill).

Figure 3 presents an SEM image of one of the meta-atom geometries of fabricated metalens. The experimental focal spot tuning is shown in Figure 4; by increasing the temperature of the fabricated metasurface, a continuous intensity modulation of the focal spot of the metalens is demonstrated, with up to 55% intensity modulation achieved by increasing the temperature from 25-125°C.

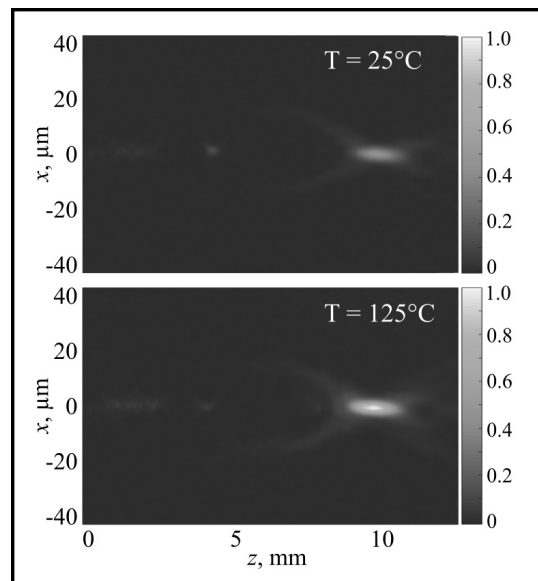


Figure 4: Experimental temperature-dependent focal spot profiles of the metalens. Top, focusing profile of the metalens at a temperature of 25°C. Bottom, focusing profile of the metalens at a temperature of 125°C.

References:

- [1] Soref, Richard. "Mid-infrared photonics in silicon and germanium." *Nature photonics* 4.8 (2010): 495.
- [2] Frey, Bradley J., Douglas B. Leviton, and Timothy J. Madison. "Temperature-dependent refractive index of silicon and germanium." *Optomechanical technologies for Astronomy*. Vol. 6273. International Society for Optics and Photonics, 2006.
- [3] Bosch, M., Shcherbakov, M. R., Fan, Z., and Shvets, G. (2019). Polarization states synthesizer based on a thermo-optic dielectric metasurface. *Journal of Applied Physics*, 126(7), 073102.

Si-on-Sapphire Metasurfaces for High Harmonic Generation and Laser Machining

CNF Project Number: 2472-16

Principal Investigator(s): Gennady Shvets

User(s): Giovanni Sartorello, Maxim Radikovich Shcherbakov

Affiliation(s): Department of Applied and Engineering Physics, Cornell University.

Primary Source(s) of Research Funding: Office of Naval Research (ONR) Grant No. N00014-17-1-2161, Air Force Office of Scientific Research (FA-9550-16-1-0069 and FA9550-16-1-0013), CCMR NSF MRSEC program (DMR-1719875)

Contact: gs656@cornell.edu, gs664@cornell.edu, mrs356@cornell.edu

Website: shvets.aep.cornell.edu

Primary CNF Tools Used: JEOL 9500, Oxford Cobra ICP, SC-4500, wet benches

Abstract:

We used a silicon-on-sapphire (SOS) platform to fabricate several metasurfaces for nonlinear optical experiments in the mid-infrared (MIR). One series of experiments aims to use the metasurfaces for high-efficiency third harmonic generation (THG) and the generation of higher-order harmonics (HHG). Another one aims to use high laser irradiance and the localized hotspots that form within nanostructures to perform nanoscale machining by accurately controlling laser-induced damage. All samples were fabricated by electron-beam lithography (EBL) performed with the JEOL 9500, e-beam deposition of a chromium mask in one of the SC-4500 evaporators, and HBr etching in the Oxford Cobra ICP etcher.

Summary of Research:

We work in nonlinear optics with sources in the MIR, and our aim is the efficient generation of optical harmonics — light with a multiple of the original MIR frequency [1]. Harmonics generation in solid-state materials is commonly used in laser systems, and has promising applications both in the sciences (such as for solid-state attosecond lasers) and in everyday life (for example in telecommunications) [2].

Nonlinear metasurfaces, planar arrays of thin subwavelength structures, have emerged as a platform for nonlinear generation and nonlinear light control [3,4]. Their parameters, such as geometric properties, refractive index and local phase profile can be adjusted to perform, in a compact form factor, functions that ordinarily require bulky materials or gases [5].

Our metasurfaces are based on dielectric resonators, rectangular silicon structures of dimensions w_x, w_y, w_z arranged in a lattice of period p_x, p_y . Adjusting these dimensions controls the resonance spectral position as well as its width, both of which must match experimental requirements. At resonance, greatly increased coupling of the fundamental light to the metasurfaces increases the amount of energy available for nonlinear processes, resulting in much increased nonlinear generation. It also changes the energy distribution of the electrons in the material, potentially with a time dependence, which, if correctly exploited, can further enhance the emission of harmonics. The result is, potentially, not only highly efficient HG in a compact, ultrathin system, but also the emission of higher-order harmonics that are normally obtained in gases.

Usually, suitable periods are a little less than the wavelength, x/y dimensions are smaller than that, and the thickness of the structures is even smaller. Deeply subwavelength thicknesses relax phase matching conditions for the generation of harmonics and prevent the harmonics themselves from being excessively reabsorbed.

We fabricate our samples starting from commercially available silicon-on-sapphire substrates. Our structures are arranged in square or rectangular arrays a few hundred μm to 1 mm to the side. We fabricate several such arrays in a grid on each sample, each with a slightly differing pattern or rescaled by a certain amount, to give a distribution of resonance wavelengths, allowing us to compare resonant and nonresonant behavior and account for slight deviations during fabrication.

Each substrate, etched down to the correct thickness in the Oxford Cobra ICP etcher with HBr, was coated in PMMA 495 A4 on a spinner, baked on the hot plates, and exposed in the JEOL 9500 EBL machine. The pattern was developed with 1:3 MIBK:IPA and a subsequent IPA wash. A Cr mask 40-50 nm thick was then deposited with one of the SC-4500 evaporators. Lift-off followed with sonication in acetone, leaving a patterned Cr mask on the bare Si. Etching around the mask down to the sapphire was again done with the Oxford Cobra. The mask was finally removed with chromium etchant in a wet bench.

This year, we fabricated several series of samples, which have been used to study THG with chirp-dependent

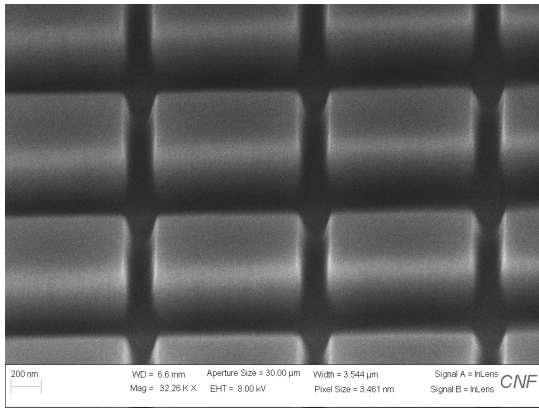


Figure 1: SEM detail of a Si nonlinear metasurface, a $1.16 \times 1.16 \mu\text{m}^2$ array of $0.99 \times 0.75 \times 0.3 \mu\text{m}^3$ structures.

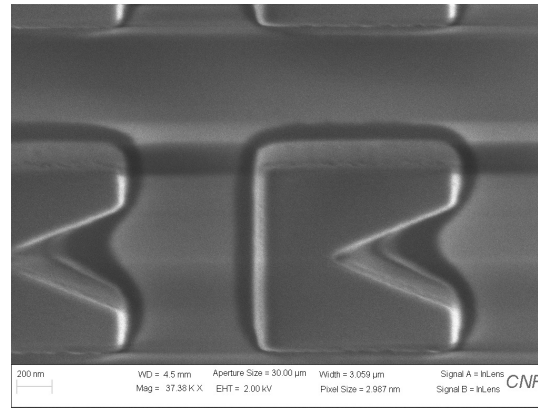


Figure 2: SEM detail of a Si laser machining metasurface, a $1.94 \times 1.95 \mu\text{m}^2$ array of $1.08 \times 1.15 \times 0.3 \mu\text{m}^3$ structures. The notch is $0.72 \mu\text{m}$ deep.

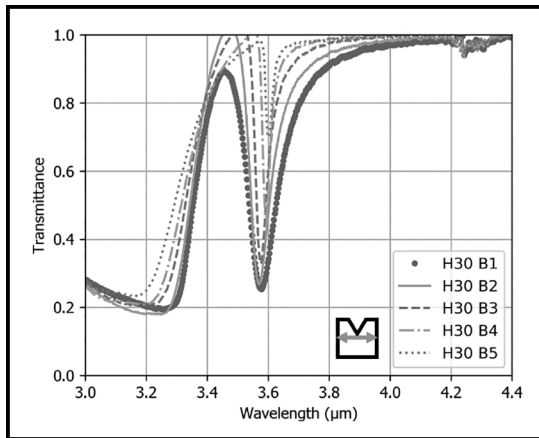


Figure 3: Transmittance FTIR spectra of the laser machining metasurface. The array detail in Figure 3 is “B1” in the legend. Inset: polarization of the incident wave.

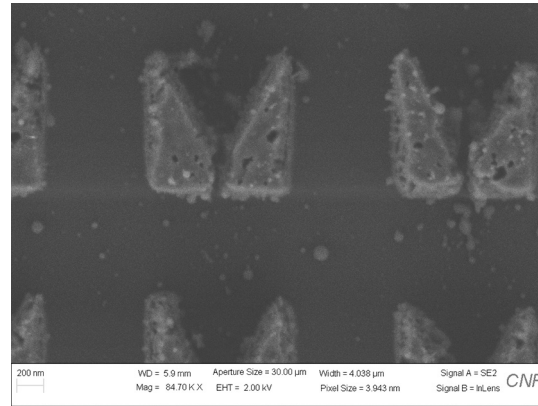


Figure 4: Early example of laser machining shown on a previously fabricated sample. Image credit: Melissa Bosch.

behavior induced by tuning the chirp of the incident pulses as well as HHG experiments. An example of a metasurface for HG is shown in Figure 1.

All HG metasurfaces are simple rectangular resonators, because there is no particular need for a more complex shape for the purposes of the project. The resonator shape, however, can be used to increase field concentration in a particular spot of the resonator. Sharp features or restriction points create hot spots, which are used extensively in nanoscale resonators. The high field concentration may cause damage, usually an unwanted problem, which we want to exploit to machine coupled resonators separated by very small gaps.

We fabricated square resonators with notches (Figure 2), then used laser pulses to cause the structures to break at the notch position, where field concentration is the highest. The resonant behavior of these structures pre-machining, which exemplifies that of all samples in this report, is shown in Figure 3.

The intended outcome is shown in a preliminary result, separately obtained on an older sample, in Figure 4.

Conclusions and Outlook:

We have successfully used a SOS platform to fabricate a number of Si resonator meta-surfaces, which we have used for a variety of nonlinear experiments in the MIR. We will continue to develop the platform to reach higher harmonic orders and greater efficiency. We have also developed a promising platform for nanoscale laser machining, whose behavior we will study and improve as necessary to achieve small, well defined and controlled features.

References:

- [1] Boyd, R. W., “Nonlinear Optics”, Academic Press, 2008.
- [2] Garmire, E., “Nonlinear optics in daily life”, Opt. Express, 21(25), 30532, 2003.
- [3] G. Li, S. Zhang, and T. Zentgraf, “Nonlinear photonic metasurfaces,” Nat. Rev. Mater., vol. 2, no. 5, p. 17010, 2017.
- [4] A. Krasnok, M. Tymchenko, and A. Al “Nonlinear metasurfaces: a paradigm shift in nonlinear optics,” Mater. Today, vol. 21, no. 1, pp. 8-21, Jan. 2018.
- [5] M. R. Shcherbakov, K. Werner, Z. Fan, N. Talisa, E. Chowdhury, and G. Shvets, “Photon acceleration and tunable broadband harmonics generation in nonlinear time-dependent metasurfaces,” Nat. Commun., vol. 10, no. 1, p. 1345, 2019.

Silicon Metasurfaces for Magneto-Optics

CNF Project Number: 2472-16

Principal Investigator(s): Gennady Shvets

User(s): Daniil Shilkin, Maxim Radikovich Shcherbakov, Melissa Bosch

Affiliation(s): School of Applied and Engineering Physics, Department of Physics; Cornell University

*Primary Source(s) of Research Funding: Office of Naval Research (ONR),
Air Force Office of Scientific Research, and National Science Foundation (NSF)*

*Contact: gs656@cornell.edu, ds2232@cornell.edu, mrs356@cornell.edu,
mb2583@cornell.edu, shilkin.daniil@physics.msu.ru*

Website: <http://shvets.aep.cornell.edu>

*Primary CNF Tools Used: JEOL 9500, Zeiss Ultra SEM, Oxford Cobra ICP Etcher,
Oxford PECVD, SC4500 Evaporator, CHA Evaporator*

Abstract:

E-beam lithography is applied to fabricate arrays of optically resonant silicon disks followed by covering them with a nickel film to be used in magneto-optical measurements.

Summary of Research:

Electron-beam lithography is often applied to produce semiconductor optical metasurfaces with a typical feature size of 100 nm or below [1,2]. Below are the results of applying this technique to fabricate dense arrays of optically resonant amorphous silicon (α -Si) disks on a glass substrate followed by covering the structure with a thin nickel film to be used in magneto-optical measurements [3]. The pattern presented three $0.5 \times 0.5 \text{ mm}^2$ arrays with a constant period of 400 nm and the varied diameter of the disks (Figure 1). The desired height of the disks was 135 nm, and the desired nickel thickness was 5 nm. The resist was hydrogen silsesquioxane (HSQ). Fused silica glasses with a thickness of 0.5 mm were used as substrates.

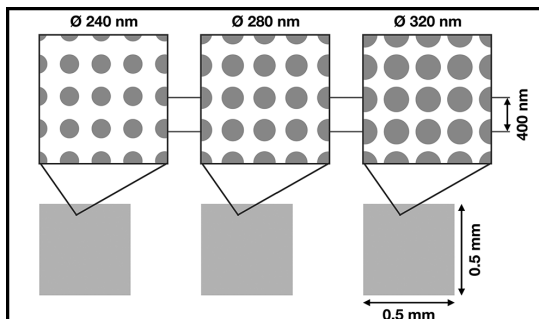


Figure 1: Scheme of the pattern.

The substrates were covered by α -Si using the Oxford plasma enhanced chemical vapor deposition (PECVD) system. The parameters were fixed at the following values: temperature 200°C, microwave power 10 W,

pressure 1 Torr, SiH_4/Ar 25/475 sccm. The deposition rate, measured close to the substrate center, was found to depend on the substrate dimensions and varied from 10.6 nm/min (for 1-inch circles) to 11.6 nm/min (for $10 \times 10 \text{ mm}^2$ squares). For the desired samples, 135 nm thick films were fabricated. The film thicknesses were measured by FilMetrics F50-EXR using the dispersion data obtained by the Woollam spectroscopic ellipsometer.

The fabricated α -Si films were covered with the resist layer by spin coating. The standard procedure resulted in a non-uniform deposition of the film: the profile of the vacuum holder appeared on the resist layer. This was overcome by placing an aluminum disk on the chuck and fixing the substrates with a Kapton® tape.

The e-beam exposure was performed using JEOL 9500. The files were prepared by standard methods including the proximity effect correction. In every session, the pattern was exposed with a number of different base doses. The other varied parameters included the beam current and the shot spacing, the resist thickness, the baking temperature and time, the choice of the charge dissipative layer, the choice of the developer, and the developing time. These parameters are discussed below.

After the pattern development, samples were etched using Oxford Cobra HBr etcher with the parameters fixed at the following values: HBr/Ar 20/7 sccm, RIE/ICP 30/1500 W, pressure 11 mTorr. The etching rate of $178 \pm 2 \text{ nm/min}$ was measured using 400-nm-thick films by etching for different times.

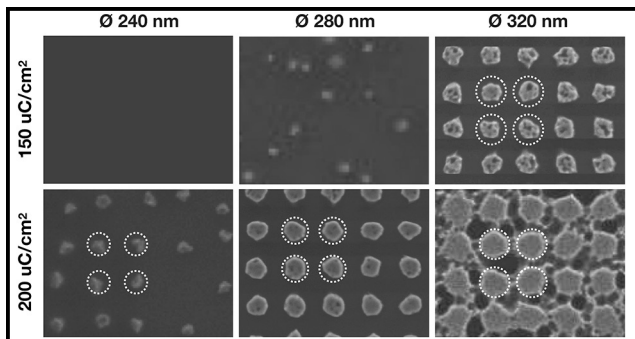


Figure 2: SEM of one of the first fabricated samples. Circles indicate the diameter set in the pattern.

For samples with the silicon thickness of 135 nm, the etching time of 50 s provided full etching outside of the mask with no cut-off. The presence of the resist residue on top of the disks was not desired, but not critical for our purpose.

The resulting structures were covered by a 5 nm nickel film using the SC4500 odd-hour evaporator. The thermal source was used with the deposition rate set to 0.5-1.0 Å/s.

Figure 2 shows scanning electron microscope (SEM) images of one of the first samples that was fabricated as follows. The 6% HSQ solution was spin coated at 3000 rpm for 60 s with the lid opened. The resist was baked at 170°C for 2 min and covered with DisCharge by spin coating at 3000 rpm for 60 s. The beam current was 1 nA; the shot spacing was 6.5 nm. The pattern was developed in 300 MIF for 2 min, rinsed in water and blow dried. The SEM images were obtained after plasma etching for 43 s and spin coating DisCharge. The fabricated disks appeared to exhibit irregular shapes with either dimensions reduced (at low doses) or disks merged (at higher doses). The optimal dose was found to depend on the diameter of the disks.

These issues were solved as follows. First, the shapes were found to be smoother when a gold film is used instead of the DisCharge. The gold was deposited after the resist baking using CHA thermal evaporator with the deposition rate set to 1.0 Å/s. Second, the use of the 'salty' developer instead of MIF 300 significantly increased the contrast of the resulted pattern. Finally, using a thinner (30 nm) resist provided the best correspondence between the set and the obtained disk diameters.

Figure 3 shows SEM images of the last sample that was fabricated as follows. The 2% HSQ solution was spin

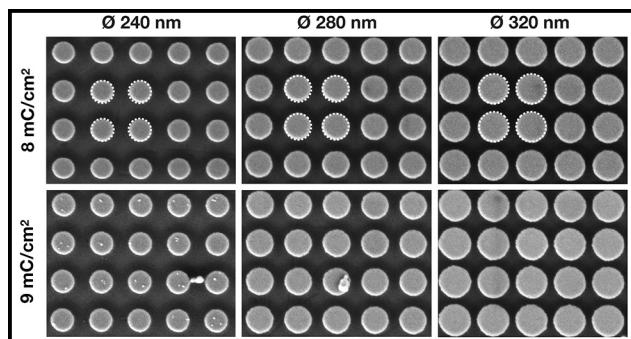


Figure 3: SEM of the last fabricated sample. Circles indicate the diameter set in the pattern.

coated at 4000 rpm for 60 s with the lid closed. The resist was baked at 115°C for 70 s and covered with a 13 nm gold film. The beam current was 20 nA; the shot spacing was 5 nm. Directly after the exposure, the gold was removed by wet etching for 30 s in gold etch, the sample was rinsed in water and put into 'salty' developer for 1 min, then rinsed in water, rinsed in isopropyl alcohol (IPA), and blow dried by nitrogen. The SEM images were obtained after plasma etching for 50 s and nickel film deposition. The fabricated disks have a smooth circular shape with the dimensions very close to the set values at a single optimal dose for all of the diameters (the size variations are less than SEM accuracy).

The established metasurface fabrication approach is scalable; thereby promising versatile platforms for ultrathin optical devices poised to find use in free-space and integrated photonics.

Acknowledgements:

This work was supported by the Office of Naval Research (ONR) under Grant No. N00014-17.1-2161, by the Air Force Office of Scientific Research (FA-9550-16-1-0069 and FA9550-16-1.0013), and by the Cornell Center for Materials Research with funding from the NSF MRSEC program (DMR-1719875).

References:

- [1] Z. Dong, et al. Nano Letters 17(12), p.7620-7628 (2017).
- [2] A. Martins, et al. Optics Express 26(8), p.9573-9583 (2018).
- [3] M.G. Barsukova, et al. ACS Photonics 4(10), p.2390-2395 (2017).

On-Chip Monolayer WSe₂ Microring Laser Operating at Room Temperature

CNF Project Number: 2524-17

Principal Investigator(s): Jaime Cardenas

User(s): Marissa Granados-Baez

Affiliation(s): The Institute of Optics, University of Rochester, Rochester, NY, 14627

Primary Source(s) of Research Funding: University of Rochester

Contact: jaime.cardenas@rochester.edu, mgranad2@ur.rochester.edu

Website: <https://www.hajim.rochester.edu/optics/cardenas/>

Primary CNF Tools Used: JEOL 9500, Logitech Orbis CMP, SÜSS MA6-BA6 contact aligner, Oxford 100 & 81 etchers

Abstract:

We demonstrate lasing at room temperature of monolayer WSe₂ integrated with a silicon nitride ring resonator. Signatures of lasing are shown by a 'kink' in the L-L plot and a linewidth narrowing of 30% when reaching threshold.

Summary of Research:

Monolayers of transition-metal dichalcogenides (TMDCs) are excellent materials to produce nanolasers since they are direct bandgap emitters and lack the need of lattice matching making them easy to integrate with planar devices. However, previously demonstrated TMDC nanolasers emit perpendicularly to the plane of their cavity into free space [1-4] and are thus challenging to integrate on chip. Integrated nanolasers are one of the key devices for fully integrated optical circuits, which require sources, modulators, and detectors interconnected with waveguides and electronics in a single chip. Modulation, detection and propagation of light have been demonstrated using TMDCs and other 2D materials. The waveguide coupled 2D material laser demonstrated here will ultimately enable photonic devices with sources, detectors, modulators, and sensors integrated in multiple photonic layers that can be monolithically integrated with electronics.

We demonstrate lasing from a monolayer tungsten diselenide (WSe₂) monolithically integrated with a high Q, chipscale silicon nitride microring resonator. This integration enables efficient light emission coupled to an on-chip waveguide. The device consists of a silicon nitride microring resonator with a radius of 13 μm coupled to a Mach-Zehnder Interferometer (MZI). We use the MZI to decrease the number of resonant modes since the gain threshold for lasing increases proportionally with the number of resonant modes of the cavity. Depending on the length of the MZI arms, resonances of the ring can be suppressed.

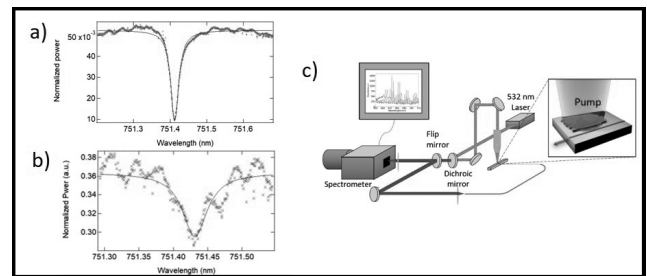


Figure 1: a) Ring resonance at 751.41nm with $Q = 350,000-200,000$. b) Ring resonance after monolayer transfer with $Q = 95,000$. c) Experimental setup to pump from the top and collect the chip's output from the side.

Our device is designed to suppress every other resonance of the ring, increasing its Free Spectral Range (FSR) by a factor of two. The width and thickness of the waveguide are 0.5 μm and 0.3 μm, respectively. The ring and bus waveguide are separated by a gap of 0.35 μm. Mechanically exfoliated WSe₂ is transferred using a PDMS-based all dry transfer technique [5] and placed on top of the microring resonator. Before the monolayer is transferred, the microring has an intrinsic Q of 350,000 (Figure 1a). After the monolayer transfer the intrinsic quality factor of the ring is 95,000 (Figure 1b) showing a strong interaction of the ring with the monolayer.

We fabricate the silicon nitride microring resonator by depositing 300 nm of silicon nitride via low-pressure chemical vapor deposition (LPCVD) on 4 μm of oxide thermally grown on a silicon wafer. The ring and bus waveguide are patterned with electron-beam lithography. A fill pattern that serves as a chemical mechanical polishing (CMP) stop layer is written with contact lithography. The nitride is etched in an inductively coupled plasma reactive ion etcher (ICP-RIE) using a CHF_3/O_2 chemistry. The device is clad with 1 μm of silicon dioxide via plasma enhanced chemical vapor deposition (PECVD). We polish the upper cladding down to a thickness of 0 to 20 nm using CMP to increase the interaction between the optical field in the resonator and the WSe_2 monolayer. The smooth surface after the CMP step also improves the adhesion of the WSe_2 flake.

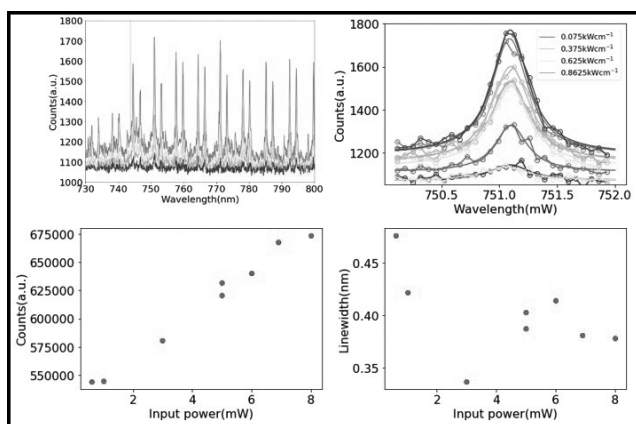


Figure 2: a) Spectrum for increasing input power. b) Lorentzian function fitting for a peak at 751.05 nm at different input powers. c) L-L plot showing a 'kink' between 1 mW and 3 mW of input power. d) Linewidth vs input power plot showing linewidth narrowing between 1 mW and 3 mW of input power.

We demonstrate optically pumped lasing emitted at a central wavelength of 751.05 nm by a monolayer of WSe_2 . We focus the pump laser (CW Ti:Sapphire at 701 nm) emission that is coupled from the ring to the bus waveguide with a lensed optical fiber at the output of the chip. The collected emission is measured with a spectrophotometer (Figure 1c). The collected spectra (Figure 2a) show the expected WSe_2 broad PL spectrum

centered at ~ 749 nm with peaks that match the ring resonances. All the measurements were done at a room temperature of 22°C.

The laser emission is identified by the behavior of the 'light-light' or L-L curve and the linewidth narrowing of particular peaks. We fitted a Lorentzian line shape to the individual peaks (Figure 2b) to obtain the FWHM values and output intensity values. The plot of the output light intensity (defined as the integrated area under the peak) vs. the input power in Figure 2c shows a 'kink' between 1 mW and 3 mW. For the same range of input power, the input vs. linewidth plot in Figure 2d shows progressive narrowing from 0.48 nm to 0.38 nm. The linewidth narrows by 30%. Linewidth narrowing indicates a laser like behavior of the emission coupled to the ring and later to the bus waveguide.

Conclusions and Future Steps:

In conclusion, our device demonstrated the possibility to integrate the photoluminescence of monolayer TMDCs and produce integrated laser emission at room temperature enabling a lasing platform that is scalable to arrays of on-chip lasers. Since integrated modulation and detection can also be achieved with 2D materials, our integrated laser opens the possibility to a fully integrated and complete optical circuit using the properties of 2D materials.

References:

- [1] Wu, S., et al. Monolayer semiconductor nanocavity lasers with ultralow thresholds. *Nature* 520, 69-72 (2015).
- [2] Ye, Y., et al. Monolayer excitonic laser. *Nature Photon.* 9, 733-737 (2015).
- [3] Li, Yongzhuo; Zhang, Jianxing; Huang, Dandan; Sun, Hao; Fan, Fan; Feng, Jiabin; Wang, Zhen; Ning, C. Z. *Nature Nanotechnology* 12,987-992 (2017).
- [4] Javerzac-Galy, J., Kumar, A., Schilling, R.D., Piro, N., Barbone, M., Goykman, I., Khurgin, J.B., Ferrari, A.C., and Kippenberg, T. J., "Excitonic emission of monolayer semiconductors near-field coupled to high-Q microresonators," arXiv preprint arXiv:1710.04294 (2017).
- [5] C.Chakraborty; K.M. Goodfellow; S.Dhara; A.Yoshimura; V.Meunier; A.N.Vamivakas *Nano Lett.* 2017, 17, 2253-2258 (2017).

Single-Shot, Multiple I/O Photonic Chip to Fiber Array Packaging Using Fusion Splicing

CNF Project Number: 2524-17

Principal Investigator(s): Jaime Cardenas²

User(s): Juniyali Nauriyal¹, Meiting Song², Jaime Cardenas²

Affiliation(s): 1. Department of Electrical and Computer Engineering, University of Rochester, Rochester, N.Y. 14627, USA; 2. The Institute of Optics, University of Rochester, Rochester, N.Y. 14627, USA

Primary Source(s) of Research Funding: Technology Development Fund, University of Rochester

Contact: jaime.cardenas@rochester.edu, jnauriya@ur.rochester.edu

Primary CNF Tools Used: GSI, furnace, ASML stepper 3000, Oxford 82, Oxford 100, Gamma

Abstract:

We show a novel multiple I/O photonic packaging method for 4-fiber array using fusion splicing. We demonstrate a minimum loss of 2.5 dB per facet with a variation of +/-0.1 dB through a 4-fiber array.

Summary of Research:

With increase in parallelism and switching in data communication and increasing integration between electronics and optics, highly efficient communication links are needed. However, packaging of integrated devices with multiple I/O ports in a single run remains a challenge. To keep up with the highly data driven communication systems, a low-cost and low-loss packaging technique for photonic integrated circuits with multiple port devices like switches, interferometers and modulators [1,2]. Current packaging methods for multiple I/O photonic chip utilize packaging of a single fiber individually. This process is inefficient while packaging many output ports, however, as the parallelism between electronics with optics increases, multiple I/O ports will be required for switching. In a silicon photonics foundry, packaging each fiber individually consumes equipment time and increases packaging cost of a single chip. We introduce a packaging technique for packaging multiple fibers (2,4) at once using a CO₂ laser to splice the fiber-array to the photonic integrated circuit.

Multiple packaging methods use special fixtures, fabrication steps and tools for aligning fiber arrays to a photonic chip, however, these methods use optical adhesive for packaging the devices which shrinks during curing and leads to misalignment losses. Most techniques also use special fixtures like v-grooves, specialized connectors or polymer lids/waveguides with optical adhesive for packaging photonic devices with multiple I/Os [3-5]. The v-grooves are used for passive alignment of the fiber to the chip, however, packaging of the fiber array is still done using optical adhesives. Optical adhesives shrink during curing and since alignment tolerances are tight, it becomes challenging to

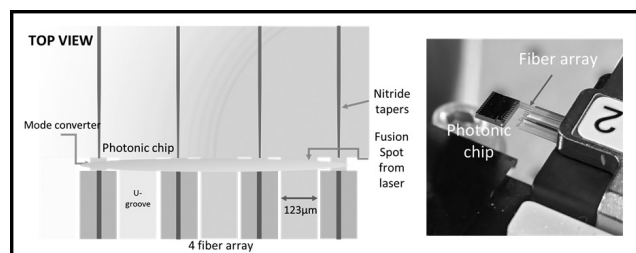


Figure 1: Left; Schematic representation of the top view of the method shows the fusion splicing spot from the CO₂ laser and the u-grooves for aligning fiber arrays. Right; A photograph of a packaged photonic device to a fiber array on a holder.

achieve low losses with high scalability. Fabrication of v-grooves requires very precise etch rates and increases fabrication steps.

We demonstrate a novel photonic packaging method for permanent optical edge coupling between a fiber-array and a photonic chip using fusion splicing which is low-loss, low-cost, robust, and scalable to high volume manufacturing without using an optical adhesive. We fabricate u-grooves on the chip for placement of fiber arrays with a pitch of 250 µm as shown in Figure 1. These u-grooves help in the placement of the fiber, which is coupled to the oxide mode converter [6]. The oxide mode converter matches the modes between a SMF-28 optical fiber (mode size of 10.4 µm) to a waveguide (mode size < 1 µm). We engineer the geometry of the two sides of the oxide mode converter to maximize the coupling from the waveguide nanotaper to the cleaved optical fiber.

We fabricate silicon nitride waveguide devices using standard CMOS compatible, microfabrication techniques. A 5 μm thick layer silicon dioxide is deposited via a plasma-enhanced chemical vapor deposition (PECVD) on the silicon wafer and 309 nm of silicon nitride are deposited via low pressure chemical vapor deposition. The waveguides are patterned with standard DUV optical lithography at 248 nm and etched using a fluorine chemistry in an inductively coupled plasma reactive ion etcher. We clad the devices with 5 μm of silicon dioxide using plasma enhanced chemical vapor deposition. We then pattern the chip structure with u-grooves and deep-etch the silicon to a depth of about 100-120 μm . After dicing, we remove the silicon substrate underneath the oxide mode converter to optically isolate it.

We fusion splice an entire fiber-array of four fibers to the mode-converter using a CO_2 laser in a single shot to achieve high manufacturing scalability. We use a cylindrical lens to focus the beam of the CO_2 laser in one dimension to a width ~ 3 mm. As the beam is focused into a line, it is aligned at the fiber to mode converter interface and then radiated with CO_2 laser for 1 sec at $\sim 10\text{W}$ of laser power. The width (3 mm) is selected to enable fusing a 12-fiber array in a single shot for future applications. Fusing multiple fibers at once significantly decreases the time and the cost involved in packaging a single chip. Fusing the fiber array and the chip together using radiative heating leaves no residue behind and forms a permanent bond, not requiring extra fixtures or adhesives for durability.

We fuse cleaved 1, 2 and 4-fiber arrays to the oxide mode converter using a single shot from the CO_2 laser and measure a coupling loss of 1.2 dB, 2.2 dB and 2.5 dB per-facet respectively. A waveguide propagation loss of 0.4 dB was subtracted from the measured loss. We expect to see a decrease in the coupling loss after the application of an optical adhesive [7]. We measure variation of ± 0.1 dB through a 4-fiber array at 1550 nm and ± 0.05 dB through a 2-fiber array at 1550 nm as shown in Table 1.

Photonic packaging has the potential to achieve manufacturing scalability at industry level using single shot fusion splicing using a CO_2 laser, which is cost and time efficient. We envision that this method can be fully automated using passive alignment techniques to enable efficient, fast and low-cost fiber array to chip packaging in high volume applications. To provide more mechanical stability, the fiber array can be fused to the chip at multiple spots eliminating the need for optical adhesives.

References:

- [1] L. Schares, B. G. Lee, F. Checcoli, R. Budd, A. Rylyakov, N. Dupuis, F. Petrini, C. L. Schow, P. Fuentes, O. Mattes, and C. Minkenberg, "A Throughput-Optimized Optical Network for Data-Intensive Computing," *IEEE Micro* 34, 52-63 (2014).
- [2] X. Wang, W. Jiang, L. Wang, H. Bi, and R. T. Chen, "Fully Embedded Board-Level Optical Interconnects from Waveguide Fabrication to Device Integration," *J. Lightwave Technol.* 26, 243-250 (2008).
- [3] T. Barwicz, N. Boyer, S. Harel, T. W. Lichoulas, E. L. Kimbrell, A. Janta-Polczynski, S. Kamalpurkar, S. Engelmann, Y. A. Vlasov, and P. Fortier, "Automated, self-aligned assembly of 12 fibers per nanophotonic chip with standard microelectronics assembly tooling," in 2015 IEEE 65th Electronic Components and Technology Conference (ECTC) (2015), pp. 775-782.
- [4] M. Papes, P. Cheben, D. Benedikovic, J. H. Schmid, J. Pond, R. Halir, A. Ortega-Moñux, G. Wangüemert-Pérez, W. N. Ye, D.-X. Xu, S. Janz, M. Dado, and V. Vanek, "Fiber-chip edge coupler with large mode size for silicon photonic wire waveguides," *Opt. Express*, OE 24, 5026-5038 (2016).
- [5] R. Hauffe, U. Siebel, K. Petermann, R. Moosburger, J.-R. Kropp, and F. Arndt, "Methods for passive fiber chip coupling of integrated optical devices," in 2000 Proceedings. 50th Electronic Components and Technology Conference (Cat. No.00CH37070) (2000), pp. 238-243.
- [6] J. Nauriyal, M. Song, R. Yu, and J. Cardenas, "Fiber-to-chip fusion splicing for low-loss photonic packaging," *Optica*, OPTICA 6, 549-552 (2019).
- [7] W. N. Ye and Y. Xiong, "Review of silicon photonics: history and recent advances," *Journal of Modern Optics* 60, 1299-1320 (2013).

No of fiber	Coupling loss per-facet (dB)	Deviation (dB)
1	1.2	0
1	2.2	(+/-)0.05
2	2.3	
1	2.5	(+/-)0.1
2	2.6	
3	2.7	
4	2.7	

Table 1: Coupling losses for 1, 2, and 4-fiber arrays.

Precise Phase Measurement with Weak Value Amplification on Integrated Photonic Chip

CNF Project Number: 2524-17

Principal Investigator(s): Jaime Cardenas

User(s): Meiting Song

Affiliation(s): The Institute of Optics, University of Rochester

Primary Source(s) of Research Funding: DRS, Andrew Jordan LLC

Contact: jaime.cardenas@rochester.edu, msong17@ur.rochester.edu

Website: <https://www.hajim.rochester.edu/optics/cardenas/>

Primary CNF Tools Used: Low pressure chemical vapor deposition (LPCVD), plasma-enhanced chemical vapor deposition (PECVD), JEOL 9500, ASML stepper, Oxford 100 ICP-RIE, AJA sputterer

Abstract:

We show, for the first time, phase measurement with weak value amplification on an integrated photonic chip. We demonstrate 9 dB improvement of signal over an on-chip Mach-Zehnder interferometer with equal amount of detected optical power.

Summary of Research:

Weak value amplification has shown the ability to make sensitive measurements with a small portion of the light signal, including beam deflection measurement of 400 frad with 63 μW out of 3.5 mW light power [1], frequency sensitivity of 129 kHz/ $\sqrt{\text{Hz}}$ with 85 μW out of 2 mW [2] and temperature sensor with 4-fold enhancement [3]. By introducing a perturbation and post-selection of the light, weak value amplification can amplify the signal to overcome technical noises, resulting in a higher signal-to-noise ratio (SNR) with less power. However, tabletop setups are space consuming and vulnerable to environmental changes. By taking this technique to the integrated photonics regime, we can largely improve its robustness and compactness, making it a good candidate for precision metrology.

We used an integrated Mach-Zehnder interferometer (MZI) followed by a multi-mode interference waveguide (MMI) (Figure 1(a)) to achieve weak value measurement. To introduce the misalignment, in other words, a spatial phase tilt in a waveguide, we designed the structure in Figure 1(b) to couple a small part of the light in TE_0 to TE_1 . This is based on the fact that the Hermite-Gaussian expansion of a free space tilted beam is mainly a combination of fundamental and first order modes [4]. Since eigenmodes of a waveguide are similar to Hermite-Gaussian modes, we applied the theory on waveguide eigenmodes TE_0 and TE_1 .

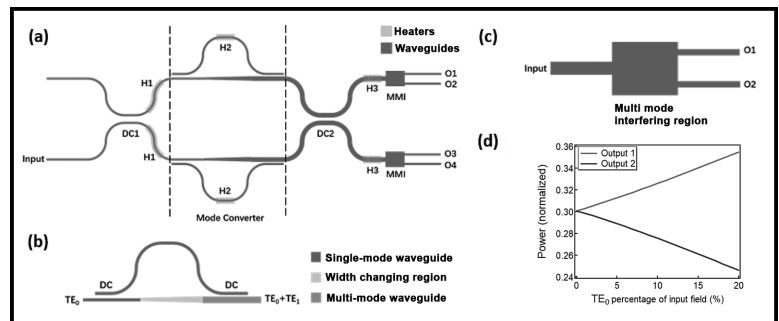


Figure 1: (a) Layout of device with heaters (not to scale). DC: direction-al coupler; H: heater; MMI: multi-mode interferometer; O: output. (b) Layout of a multimode interferometer. (c) Layout of a multi-mode interferometer. (d) Output power of MMI vs ratio of TE_0 and TE_1 mode.

We design a multimode coupler to couple light from fundamental mode to higher order mode. As shown in Figure 1(b), the lower waveguide is a single mode waveguide, which transits to a multimode waveguide through an adiabatic taper. The upper waveguide couples a slight portion of light from TE_0 in lower waveguide. Then it couples back in to the lower waveguide, but to TE_1 mode, since the TE_1 mode supported by the lower waveguide is designed to be phase matched with TE_0 in the upper waveguide.

Another necessary component is needed to measure the “location shift” at the dark port, which translates to measuring the ratio of TE_0 and TE_1 modes. We used an MMI (multi-mode interferometer, Figure 1(c)) as simulation (Figure 1(d)) shows that its output power is dependent on the ratio of the input TE_0 and TE_1 modes.

We then fabricated the device with CMOS-compatible processes. The fabrication started with a 4-inch silicon wafer with 4 μm of thermally grown silicon dioxide. We deposited a layer of 289 nm silicon nitride with low pressure chemical vapor deposition (LPCVD). Then we used e-beam lithography to pattern the waveguides and etched the silicon nitride with inductively coupled plasma reactive ion etching (ICP-RIE). As cladding on the waveguides, we deposited 2.6 μm of silicon dioxide with plasma enhanced chemical vapor deposition (PECVD). Finally, we sputtered 100 nm of platinum with lift-off method for heaters.

We compare our weak value device with a standard on-chip MZI with same footprint working in quadrature. We launch 1 mW of laser power at 1570 nm with a tapered optical fiber. The phase signal is introduced by applying a modulated 1V, 10 kHz voltage to the heater 1. The outputs are imaged onto a balanced detector and we measure the signal on an RF spectrum analyzer.

We demonstrate 9 ± 1.9 dB signal improvement over the regular MZI in the weak value device with equal amount of detected optical power. When detected powers are 14 μW , weak value device has a signal of 66.17 dBm, while the regular MZI shows 75.33 dBm. For the regular MZI to also show a signal of 66.17 dBm, it requires a higher detected power of 40.5 μW .

Conclusions and Future Steps:

In conclusion, we have shown that on-chip weak value device is a good candidate for phase related metrology, including temperature drift and frequency shift. As it provides higher signal with same amount of optical power, it can monitor the optical signal in a system without consuming a large portion of the light. On the other hand, in a detector saturation limited system, weak value device is able to further increase the signal.

References:

- [1] P. B. Dixon, D. J. Starling, A. N. Jordan, and J. C. Howell, "Ultrasensitive Beam Deflection Measurement via Interferometric Weak Value Amplification," *Phys. Rev. Lett.* 102, 173601 (2009).
- [2] D. J. Starling, P. B. Dixon, A. N. Jordan, and J. C. Howell, "Precision frequency measurements with interferometric weak values," *Phys. Rev. A* 82, 063822 (2010).
- [3] L. J. Salazar-Serrano, D. Barrera, W. Amaya, S. Sales, V. Pruneri, J. Capmany, and J. P. Torres, "Enhancement of the sensitivity of a temperature sensor based on fiber Bragg gratings via weak value amplification," *Opt. Lett.*, OL 40, 3962-3965 (2015).
- [4] J. Steinmetz, K. Lyons, M. Song, J. Cardenas, and A. N. Jordan, "Precision frequency measurement on a chip using weak value amplification," in *Quantum Communications and Quantum Imaging XVII* (International Society for Optics and Photonics, 2019), Vol. 11134, p. 111340S.

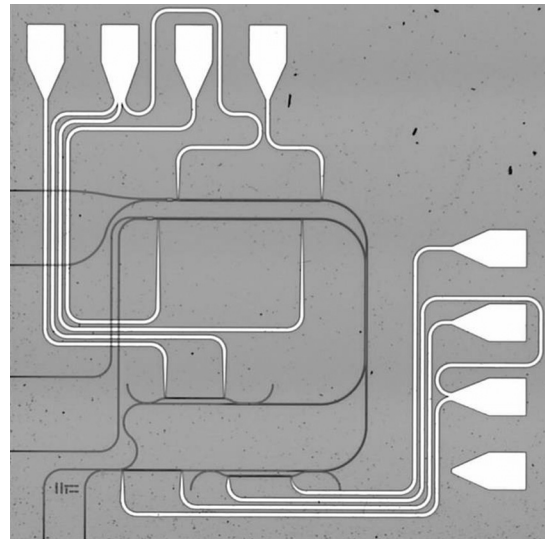


Figure 2: Microscope capture of the device. The device is wrapped around to reduce footprint.

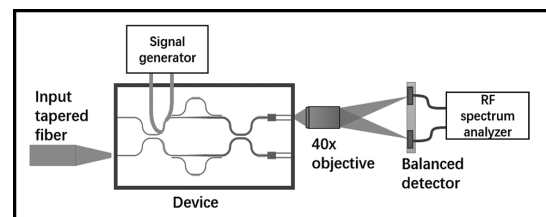


Figure 3: Illustration of testing setup.

High Transmission Plasmonic Metasurfaces in the Visible Band

CNF Project Number: 2525-17

Principal Investigator(s): Chunlei Guo

User(s): Jihua Zhang, Ran Wei

Affiliation(s): The Institute of Optics, University of Rochester

Primary Source(s) of Research Funding: Bill and Melinda Gates Foundation (OPP1119542)

Contact: chunlei.guo@rochester.edu, jzh119@ur.rochester.edu, rwei@ur.rochester.edu

Website: <http://www2.optics.rochester.edu/workgroups/guo/about.html>

Primary CNF Tools Used: JEOL 9500

Abstract:

Metasurfaces are two-dimensional nanoantenna arrays that can control the propagation of light at will. In particular, plasmonic metasurfaces feature ultrathin thicknesses, ease of fabrication, field confinement beyond the diffraction limit, and ultrafast performances. However, the technological relevance of plasmonic metasurfaces operating in the transmission mode at optical frequencies is questionable due to their limited efficiency. The state-of-the-art efficiency of geometric plasmonic metasurfaces at visible and near-infrared frequencies, for example, is $\leq 10\%$. Here, we report a multipole-interference-based transmission-type geometric plasmonic metasurface with a polarization conversion efficiency that reaches 42.3% at 744 nm, over 400% increase over the state of the art. The efficiency is augmented by breaking the scattering symmetry due to simultaneously approaching the generalized Kerker condition for two orthogonal polarizations. In addition, the design of the metasurface proposed in this study introduces an air gap between the antennas and the surrounding media that confines the field within the gap, which mitigates the crosstalk between meta-atoms and minimizes metallic absorption.

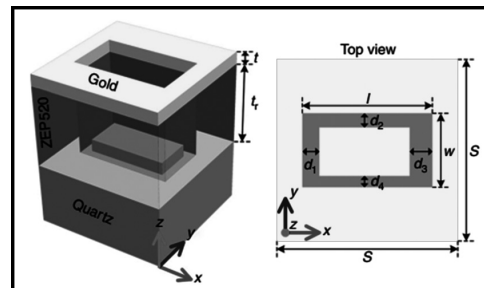


Figure 1: Schematic showing the designed multipole meta-atom, which consists of a gold nanoaperture and a gold nanorod separated by a perforated ZEP520 layer. In the meta-atom, $S = 320$ nm, $l = 230$ nm, $w = 130$ nm, $t = 35$ nm, and $t_r = 180$ nm. The multipole response of this meta-atom can be tuned by introducing an air gap between the nanorod and ZEP520 sidewalls, i.e., a noncomplementarity between the nanorod and the nanoaperture. The dimension of the air gap is denoted by $d_{1,2,3,4}$ in four sides.

Summary of Research:

In this work [1], we use multipole meta-atoms that support not only electric dipole and magnetic dipole but also an electric quadrupole and a magnetic quadrupole to construct an ideal half-wave plate. In multipole meta-atoms, it is possible to completely suppress backscattering for both orthogonal polarizations by satisfying the so-called generalized Kerker condition [2] and maintain the π -phase difference. We propose a multipole meta-atom design consisting of a metallic nanoaperture and a metallic nanorod separated by a perforated dielectric layer, as shown in Figure 1. The dimension of the nanorod and thus the multipole response can be modified by introducing a small air gap between the nanorod and the dielectric spacer separating adjacent meta-atoms, i.e. non-complementarity.

We also explore the advantages of the noncomplementary design of meta-atoms compared with complementary design, i.e. with no airgap between the nanorod and the nanoaperture. First, the introduction of non-complementarity is the key to engineering the multipole interference and enhancing the transmittance of light with cross-polarization ($T_{\text{cross-CP}}$), which, in most applications, is preferred for wavefront control of the transmitted light. As a result, we achieve an overall enhancement in the $T_{\text{cross-CP}}$ of the noncomplementary design. The peak efficiency is increased to 45.5% at a peak wavelength of 751 nm, i.e., $T_{\text{cross-CP}}$ is increased by $> 10\%$ compared with complementary design.

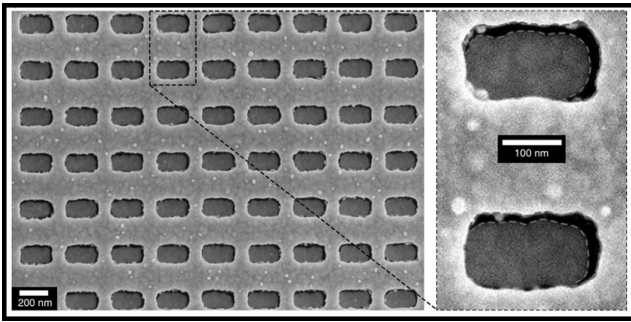


Figure 2: SEM image of a fabricated MPM and an enlarged view of two meta-atoms. The dashed lines mark the edges of the air gap.

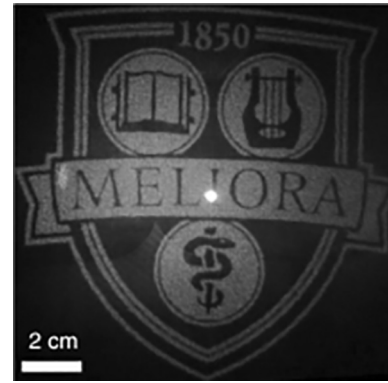


Figure 3: Holography images at 750 nm for the noncomplementary design. (See pages vi-vii for full color version.)

Another evident advantage is the reduced near-field coupling between the meta-atoms. Both designs support good orientation-controlled phase responses. However, the $T_{cross-CP}$ amplitude of the complementary design significantly changes as a function of orientation angle of the meta-atom, while the noncomplementary meta-atom has higher and relatively flat amplitudes, representing reduced field coupling between meta-atoms.

Figure 2 shows scanning electron microscopy (SEM) images of the fabricated noncomplementary metallic plasmonic metasurfaces (MPM) using e-beam lithography on JEOL 9500 at CNF. The MPM has also been further tested on two applications, a beam deflector and a hologram, respectively. The beam deflector is realized by introducing a phase gradient on the surface, here the unit cell we used consists of eight subunits with an orientation step of 22.5° . The measured extinction ratio (ER) peaks at 7.8 dB at ~ 745 nm and exceeds 0 dB between 660 and 850 nm.

Both the peak transmission efficiency (E_p) and ER are significantly higher than the values of the current state-of-the-art MPMs ($E_p \leq 10\%$, $ER \leq 0$ dB) in the visible and near-infrared regions in realizing various functionalities [3].

Another application that we demonstrate with the proposed design is a high efficiency hologram. Figure 3 shows experimental holography images in the far field at $\lambda = 750$ nm obtained from a noncomplementary design. The hologram efficiencies are measured to be 37%, which is better than those of the state-of-the-art GMs in the visible and near infrared regions [4]. The hologram is broadband as well, which shows holography images at various wavelengths.

Conclusions and Future Steps:

A significant increase in the transmission efficiency of plasmonic geometric metasurfaces is facilitated by

tuning the multipole response of individual meta-atoms and by minimizing the crosstalk between meta-atoms. The maximum efficiency of the metasurfaces is on the long-wavelength side of the visible spectrum, 744 nm.

However, the demonstrated high efficiency exceeds that of the state-of-the-art over a wide wavelength range of 630-970 nm, i.e., in the red color range of the visible (visible covers 380-780 nm) and near-infrared regions. This concept and these techniques can be used for shorter visible wavelengths or longer-wavelength regions by tuning the dimensions of the meta-atom. This concept can be used for dielectric metasurfaces as well.

Furthermore, reflective-type metasurfaces can benefit from the generalized Kerker, no-front-scattering condition. On the other hand, perfect and selective light absorption can be achieved by eliminating both reflection and transmission, using the generalized Kerker approach.

In the future, even higher-order multipoles can also be included to improve the performance of MPMs [5].

References:

- [1] Zhang, Jihua, et al. "Plasmonic metasurfaces with 42.3% transmission efficiency in the visible." *Light: Science and Applications* 8.1 (2019): 1-13.
- [2] Liu, W., and Kivshar, Y. S. Generalized Kerker effects in nanophotonics and metaoptics [Invited]. *Opt. Express* 26, 13085-13105 (2018).
- [3] Wen, D. D., et al. Metasurface for characterization of the polarization state of light. *Opt. Ex.* 23, 10272-10281 (2015).
- [4] Wan, W. W., Gao, J., and Yang, X. D. Metasurface holograms for holographic imaging. *Adv. Opt. Mater.* 5, 1700541 (2017).
- [5] Kruk, S., et al. Invited article: broadband highly efficient dielectric metadevices for polarization control. *APL Photonics* 1, 030801 (2016).

Description of the Exploratory Etching and Electrodeposition Project

CNF Project Number: 2527-17

Principal Investigator(s): Dr. David Crouse

User(s): Golsa Mirbagheri

Affiliation(s): Electrical and Computer Engineering Department, Clarkson University

Primary Source(s) of Research Funding: CFM, Clarkson University

Contact: dcrouse@clarkson.edu, mirbagg@clarkson.edu

Primary CNF Tools Used: Oxford 82, Oxford 100, ASML, Gamma, PECVD, Cobra

Abstract:

This project is a continuing project. We will be finishing the fabrication of the hyperbolic metamaterial structure and designing a 2nd generation of the filter that uses more of a photonics crystal resonant material within a Bragg stack. Both the hyperbolic metamaterial structure and the 2nd generation devices have compelling properties. Both show very little dispersion — meaning that their performance is not affected by the angle of incidence to the optical signal.

Summary of Research:

During the last year, we have further designed the hyperbolic metamaterial device and have performed much more optimization and have taken into account practical design considerations. We are now fabricating the structure at the Cornell NanoScale Science and Technology Facility (CNF) at Cornell University.

We have developed a fabrication plan and are now implementing the plan, with masks designed and fabrication processes in development. Based on what we have learned, we are now investigating a 2nd generation device that does not use metal wires, but uses resonant cavities in the three middle layers of the Bragg stack. The resulting structure will have far less polarization dependence, will absorb less radiation, will be far easier to fabricate and manufacture, and will have a larger tuning range that allows for it to be used within pixelated wavelength filters for hyperspectral imaging applications.

We have been performing preliminary testing on the resonant cavities and have a preliminary design for operation in the midwavelength infrared range of 3-5 μm . The Bragg stack will use silicon and silicon dioxide, and potentially silicon nitride — all CMOS compatible devices — as well as having all structure features with sizes amenable to optical lithography.

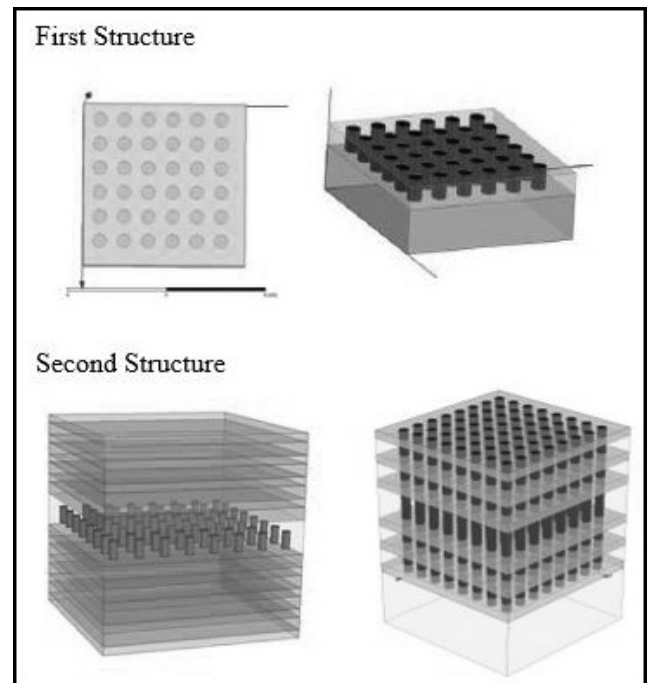


Figure 1: First Structure: The 1.5 μm SiO_2 film was deposited, patterned and etched. The holes were 0.5 μm , electroplated with Cu. Second Structure: Alternative layers of SiO_2 and Si are deposited, patterned and etched (all through the layers), then holes electroplated with Cu.

Metamaterial Spectrometer: A Low SWaP, Robust, High Performance Hyperspectral Sensor for Land and Atmospheric Remote Sensing

CNF Project Number: 2661-18

Principal Investigator and User: Lori Lepak

Affiliation(s): Phoebus Optoelectronics LLC

Primary Source(s) of Research Funding: National Aeronautics and Space Administration (NASA)

Contact: llepak@phoebusopto.com

Website: www.phoebusopto.com

Primary CNF Tools Used: ASML DUV stepper, Oxford 81 etcher, Logitech CMP, Zeiss Supra SEM

Abstract:

Since 2003, Phoebus Optoelectronics has enabled custom R&D solutions in the fields of Plasmonics, Metamaterials, Antennas, and Sensors. We work closely with our customers throughout device development, from simulation and design, to prototype realization, testing, and small volume manufacturing. Our R&D portfolio spans the spectral ranges of visible light, infrared, terahertz, and microwave radiation, for applications in high resolution imaging systems, wavelength and polarization filtering, tunable optical components, beam forming and steering, solar cells, renewable energy devices, and chemical and biological toxin sensors. We routinely partner with large, industry-leading businesses to develop products in all of these areas, jointly performing advanced testing and working together to scale up to medium- and large-volume manufacturing. Our agile team makes extensive use of the resources at the CNF for our nano/micro fabrication and testing, to provide cost efficiency and rapid turnaround.

In the present report, we discuss the ongoing development of a metamaterial-based hyperspectral imaging filter.

Summary of Research:

Phoebus uses the resources of the CNF to fabricate plasmonic chips patterned with a metamaterial surface to enable Extraordinary Optical Transmission (EOT), a phenomenon unique to metastructures in which light is transmitted through apertures much smaller than the incident wavelength, at anomalously large intensities relative to the predictions of conventional aperture

theory. EOT was first observed by T.W. Ebbesen in 1998 [1]. Since its founding in 2003, Phoebus has successfully harnessed EOT by incorporating metasurfaces into devices used to perform light filtering [2,3], photon sorting [4,5], polarimetric detection [6], high speed optical detection [7], and SPR plasmonic sensor chips [8].

In our current project, we are developing a hyperspectral imaging system, shown schematically in Figure 1. Our technology (Figure 1b) uses a metasurface to precisely target very narrow spectral bands of interest, enabling a significant reduction in the size and number of optical components relative to current state-of-the-art imaging systems (Figure 1a), which in turn will enable integration of our high-performance sensor onto weight-sensitive platforms (i.e., satellites) far more readily than existing systems. Our initial goal is to detect and image trace gases in the Earth's atmosphere in the midwave infrared (MWIR) region (defined as 3-5 μm wavelength), while reducing adjacent channel latency to less than 10 ms.

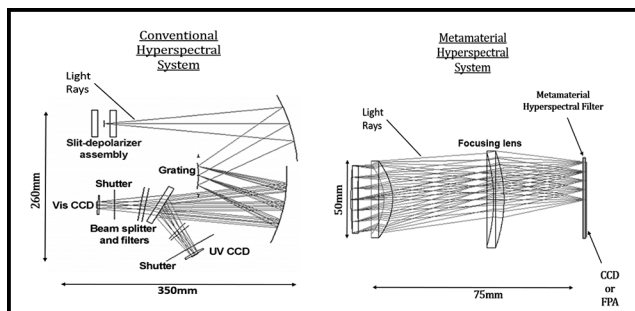


Figure 1: Phoebus's Metamaterial Spectrometer (MS) technology (right) eliminates much of the size and weight of conventional hyperspectral spectrometer technologies (left). Note the significant difference in scale of the two images.

Using the ASML DUV stepper, an entire wafer can rapidly be lithographically patterned with arrays of metastructures, as shown in Figure 2. In general, the optimal feature size and period of these metastructures depends primarily upon the desired wavelength of operation and the refractive indices of the constituent materials. In the MWIR, typical feature sizes are on the order of $\sim 1 \mu\text{m}$. As we can see in the optical microscope image in Figure 3, the ASML can easily produce highly uniform, large-area arrays of test features of an appropriate size. Equally critical for photonics applications, relatively narrow spaces between these features can be etched with moderately high aspect ratios, to form structures with nearly vertical sidewalls, as shown in Figure 4. These vertical structures both minimize optical losses, and ensure that the real fabricated devices will perform as closely as possible to the optimal designs predicted by simulations.

Conclusions and Future Steps:

Our overall metasurface technology can be easily adapted to other spectral ranges, from the visible to the microwave, by substituting appropriate materials, and scaling feature sizes in proportion to the desired wavelength of imaging. In addition to fabricating the MWIR device, we have completed the design of a visible-wavelength counterpart of the current technology, and are about to begin fabrication using all of same tools as the MWIR project, plus the Oxford PECVD and AJA sputter tool to deposit the thin films. Thus, the extensive resources of the CNF are enabling us to rapidly develop our Metamaterial Spectrometer technology for a broad range of imaging and sensing applications.

References:

- [1] Ebbesen, T.W., et al., "Extraordinary optical transmission through sub-wavelength hole arrays." *Nature*, (1998). 391(6668): p. 667-669.
- [2] Crouse, D. "Numerical modeling and electromagnetic resonant modes in complex grating structures and optoelectronic device applications." *Electron Devices, IEEE Transactions on* 52.11 (2005): 2365-2373.
- [3] Crouse, D., and Keshavareddy, P. "Polarization independent enhanced optical transmission in one-dimensional gratings and device applications." *Optics Express* 15.4 (2007): 1415-1427.
- [4] Lansley, E., Crouse, D., et al. "Light localization, photon sorting, and enhanced absorption in subwavelength cavity arrays." *Optics Express* 20.22 (2012): 24226-24236.
- [5] Jung, Y.U; Bendoy, I; Golovin, A.B.; and Crouse, D.T. "Dual-band photon sorting plasmonic MIM metamaterial sensor." *Proc. SPIE 9070, Infrared Technology and Applications XL, 90702X* (June 24, 2014); doi:10.1117/12.2050620.
- [6] Crouse, D., and Keshavareddy, P. "A method for designing electromagnetic resonance enhanced silicon-on-insulator metal-semiconductor-metal photodetectors." *J. of Optics A: Pure and Applied Optics* 8.2 (2006): 175.
- [7] Mandel, I.; Gollub, J.; Bendoy, I; Crouse, D. Theory and Design of a Novel Integrated Polarimetric Sensor Utilizing a Light Sorting Metamaterial Grating. *Sensors Journal, IEEE*, (2012): Vol. PP, 99.
- [8] Lepak, L., et al. "Handheld chem/biosensor using extreme conformational changes in designed binding proteins to enhance surface plasmon resonance (SPR)" *Proc. SPIE 9862, Advanced Environmental, Chemical, and Biological Sensing Technologies XIII, 9862-7* (April 17, 2016); doi:10.1117/12.2222305.

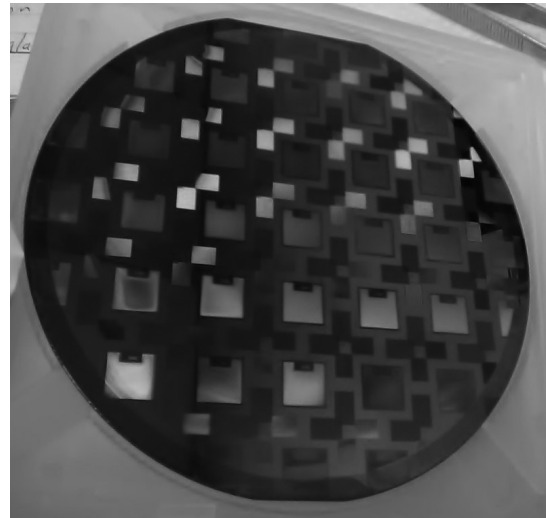


Figure 2: Wafer lithographically patterned with optical metastructures, using the ASML DUV stepper. (See pages vi-vii for full color version.)

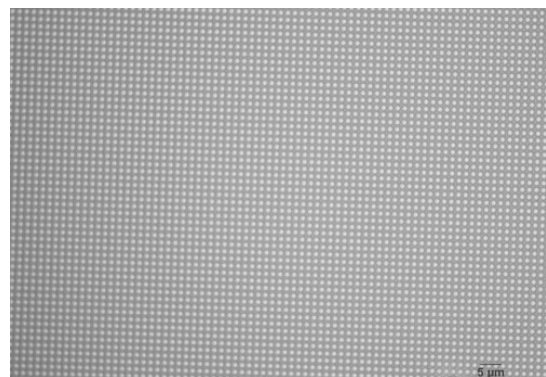


Figure 3: Optical microscope image of test pattern of array of $\sim 1 \mu\text{m}$ pillars, lithographically patterned on the ASML DUV stepper.

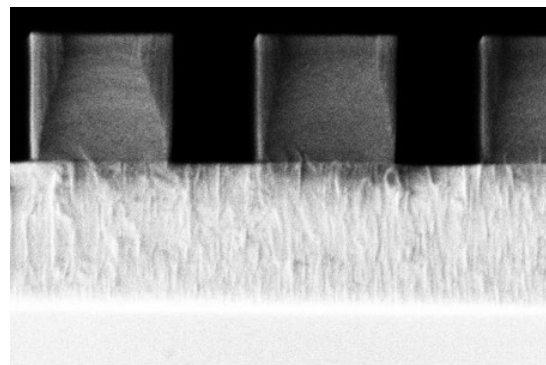


Figure 4: SEM image (cross section) of etched pillars with near-vertical sidewalls. Imaged at $\sim 90 \text{ kX}$ in the Zeiss Supra SEM, the grain structure of the etch stop layer is clearly visible.

Metasurface-Integrated Graphene for Mid-Infrared Optical Devices

NF Project Number: 2472-16

Principal Investigator(s): Gennady Shvets

User(s): Aditya Mahalanabish, Minwoo Jung

Affiliation(s): School of Applied and Engineering Physics, Department of Physics; Cornell University

Primary Source(s) of Research Funding: Office of Naval Research (ONR) and National Science Foundation (NSF)

Contact: gs656@cornell.edu, am2952@cornell.edu, mj397@cornell.edu

Website: <http://shvets.aep.cornell.edu>

Primary CNF Tools Used: JEOL 9500, CVC SC4500 evaporator, Zeiss Supra/Ultra SEM, PT740 or Anatech resist strip

Abstract:

Plasmonic metasurfaces, when integrated with graphene, can greatly enhance the absorption of incident radiation into graphene through resonant field enhancement. This metasurface structure can be obtained simply by patterning graphene itself, or it may take a form of thin metallic film periodically patterned on graphene. The former approach was used to achieve an on/off notch filter of mid-infrared radiation with narrow linewidth, and the latter approach was used to make a high-responsivity and ultrafast graphene photodetector.

Summary of Research:

Graphene Based Mid-IR High Q Active Notch Filter.

Graphene's high electronic mobility and ultrawide tunability owing to the linear Dirac electronic dispersion makes it an exceptional candidate for optoelectronic applications. However, its inherent weak absorption of only 2.3% of normally incident light in the visible and infrared spectrum acts as a bottleneck. To enhance its optical absorption, we can make use of the strong absorption properties of localized surface plasmon resonance (LSPR) in graphene. Nanopatterning of monolayer graphene using e-beam lithography and subsequent etching using RIE or FIB can be used to produce structures like nanorings and nanodisks [1], which support LSPR and have been reported to show an enhanced absorption of 25% [2]. For our structure, shown in Figure 1], we design a nano patterned graphene structure that maintains electrical connectivity and thus foregoes the requirement of an ion gel layer [1,2] — reducing the complexity in fabricating and handling such an optoelectronic device.

The device is fabricated in a total of four steps: (1) gold alignment marks and electrodes are deposited on CaF_2 (the substrate), (2) the heterostructure of graphene/hBN/graphene is transferred on to the substrate carefully to make sure each graphene layer is connected to one set of electrodes only, (3) the resonator pattern is etched on the top graphene using e-beam lithography, and (4) the graphene is etched through the developed PMMA, to get the required pattern using PT740 or the Anatech resist strip.

Figures 1 and 2 show two different fabricated resonator designs for the device. Device fabrication is at the stage of optimizing the etch recipe for graphene.

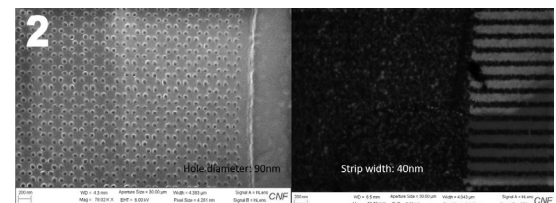
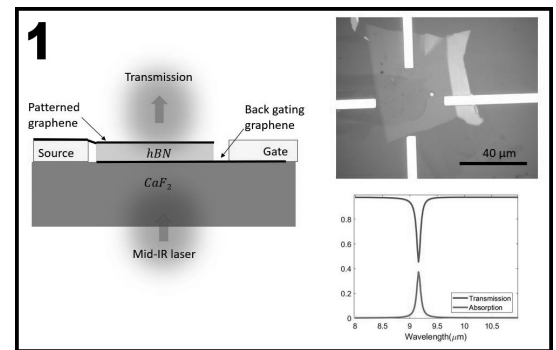


Figure 1, top: Left, schematic of the mid-IR notch filter showing the heterostructure stack. Top right, fabricated device under optical microscope, the opaque material visible in between the electrodes is the hBN layer. Bottom right, simulated mid-IR spectra of the fabricated device with the top graphene having a hexagonal pattern of holes (see Figure 2).

Figure 2, bottom: Left, SEM of developed pattern of hexagonal lattice of holes on PMMA covering the top graphene before plasma etch. Right, SEM of another possible 1D resonator pattern, rectangular strips etched on graphene, transferred on Si/SiO_2 substrate.

Graphene Photodetector with High Responsivity Enhanced by Plasmonic Metasurface. In a similar way, we resonantly boost the absorption into graphene by integrating a gold metasurface with graphene.

While graphene photodetectors enhanced by plasmonic metasurfaces are previously demonstrated [3], we aim for even greater enhancement by (1) interdigitating the source and drain and (2) using high-quality exfoliated graphene. Especially, the latter advancement is expected to give a huge improvement on the quality of detector performance, as the previous works were mostly done with CVD graphene with lower quality.

As depicted in the Figure 3 inset, we place graphene-hBN stack on top of the pre-fabricated gold metasurface structures deposited on SiO_2 -Si substrate. The gold metasurfaces are fabricated by using e-beam lithography. We use PMMA for the e-beam resist, and deposit 7 nm of Cr and 43 nm of gold using CVC SC4500 evaporators.

The device is under characterization, and here we report on its optical characterization. The photocurrent measurement is to be done in a near future.

Figure 3 shows the reflection spectra of the gold metasurfaces with and without the graphene-hBN stack. While there are some modifications to the resonance structure due to the phonon bands of hBN, the original reflection dips are well-conserved. Thus, we expect that the absorption enhancement would be maintained at the similar order of magnitude even under the perturbation by hBN. We introduce this additional hBN layer for better graphene quality. The current experiment will be followed by the electrical characterization of the devices.

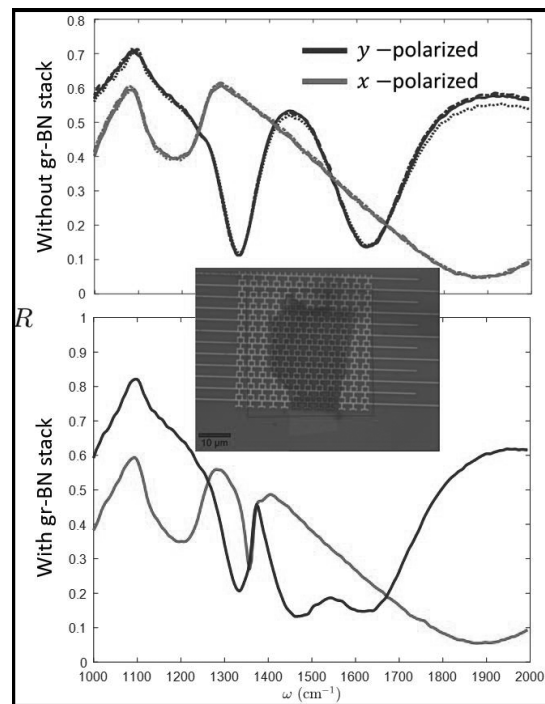


Figure 3: Optical characterization of photodetector device. Top, reflection spectra without graphene-BN stack on top of metasurface. Bottom, reflection spectra with graphene-BN stack on top of metasurface. Inset (middle), an optical microscopy image of a device with graphene-BN stack.

References:

- [1] Fang, Z. Y.; Thongrattanasiri, S.; Schlather, A.; Liu, Z.; Ma, L. L.; Wang, Y. M.; Ajayan, P. M.; Nordlander, P.; Halas, N. J.; de Abajo, F. J. G. Gated Tunability and Hybridization of Localized Plasmons in Nanostructured Graphene. *ACS Nano*, 7, 2388-2395 (2013).
- [2] Fang, Z.; Wang, Y.; Schlather, A. E.; Liu, Z.; Ajayan, P. M.; de Abajo, F. J. G.; Nordlander, P.; Zhu, X.; Halas, N. J. Active Tunable Absorption Enhancement with Graphene Nanodisk Arrays. *Nano Lett.*, 14, 299-304 (2013).
- [3] Y. Yao, R. Shankar, P. Rauter, Y. Song, J. Kong, M. Loncar, and F. Capasso; High-Responsivity Mid-Infrared Graphene Detectors with Antenna-Enhanced Photocurrent Generation and Collection. *Nano Letters* 14 (7), 3749-3754 (2014).

III-N Photonic Devices

CNF Project Number: 2801-19

Principal Investigator(s): Debdeep Jena

User(s): Kevin Lee, Shyam Bharadwaj, Ryan Page, Jimmy Encomendero

Affiliation(s): Electrical and Computer Engineering, Materials Science Engineering; Cornell University

Primary Source(s) of Research Funding: National Science Foundation

Contact: djena@cornell.edu, sb2347@cornell.edu, kl833@cornell.edu, rlp238@cornell.edu, jje64@cornell.edu

Primary CNF Tools Used: ABM contact aligner, electron-beam evaporators, Plasma-Therm inductively coupled plasma reactive ion etcher (PT 770), electron-beam lithography, atomic layer deposition, plasma-enhanced chemical vapor deposition

Abstract:

Lifi communication using III-Nitrides visible light sources has drawn huge attention recently. Our goal is to build monolithic integration of field effect transistor (FET) with blue light emitting diodes (LEDs). We use plasma-assisted molecular beam epitaxy (PA-MBE) to grow a buried tunnel junction blue LED with a n-i-n channel sitting on top. The resulting device we called “light emitting FET (LEFET)” shows successful gate modulation and on/off ratio of five orders. Light output signal can be switched up to 30 kHz.

Summary of Research:

The LEFET structure is grown on a n-type metal polar free-standing GaN substrate with dislocation density $\sim 10^6 \text{ cm}^{-2}$ by PA-MBE. The detailed structure is presented in Figure 1(a). First, a 125 nm Si-doped GaN layer is grown with $[\text{Si}] = 10^{19} \text{ cm}^{-3}$. After initial n-GaN layer, p-GaN with Mg doping of $3 \times 10^{19} \text{ cm}^{-3}$. This completes the buried tunnel junction for hole injection. The active region contains three periods of InGaN multiple quantum wells (MQWs) with blue emission at 467 nm. Later, the n-i-n FET region is grown using unintentional doped GaN (uid-GaN) sandwiched between two n-GaN layers.

The sample was processed into devices consisting of various numbers of vertical n-FET nanowires or fins of varying dimensions on top of $55 \times 55 \mu\text{m}^2$ LED mesas.

A schematic of a processed nanowire LEFET is shown in Figure 1(b). First, $55 \times 55 \mu\text{m}^2$ LED areas were isolated through inductively-coupled plasma reactive ion etching (ICP-RIE) down to the n⁺GaN nucleation layer. Next, nanowires and fins were defined on the mesa surface through electron beam lithography (EBL).

The etch process for nanowire/fin definition consisted of first an ICP etch (using Cr/Pt as an etch mask as well as top source contact) followed by a wet etch in AZ400K to make the sidewalls vertical for efficient lateral gating (see Figure 1(c)). The fins were defined with long

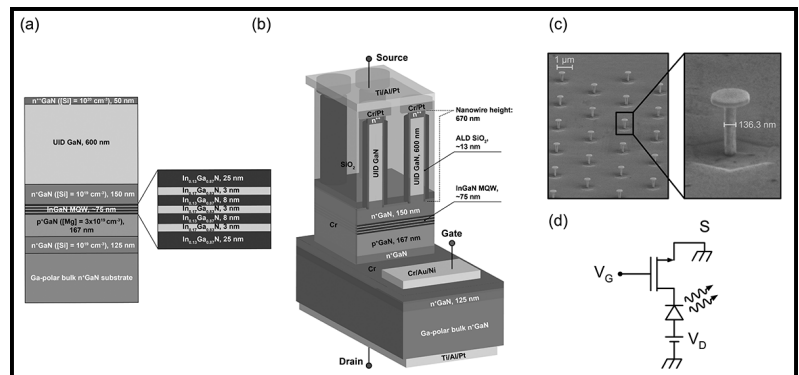


Figure 1: (a) Schematic epitaxial layer structure for the device discussed in this study. The structure consists of a vertical n-i-n GaN FET sitting above a bottom-TJ homojunction InGaN LED. (b) Schematic of a fabricated nanowire LEFET structure, showing source, gate, and drain contacts for biasing the device, and dielectrics for isolation. (c) SEM image of the nanowire LEFET structure. (d) Circuit diagram of the LEFET.

edge along the m-plane direction in order to allow for adequate wet etching. Then, SiO₂ was deposited by atomic layer deposition (ALD) as a gate dielectric for the nanowire/fin FETs.

Next, Cr was sputtered as the sidewall gate metal, followed by e-beam evaporation of large Cr/Au/Ni pads for electrically contacting the gate. The undesired sputtered Cr above the source contact of the fins and wires was etched away after a planarization process, after which SiO₂ was blanket deposited by plasma-enhanced chemical vapor deposition (PECVD) to isolate

the rest of the sidewall gate metal. This SiO₂ was then planarized to again expose the Cr/Pt wire/fin source contact, after which thick source pads (Ti/Al/Pt) for probing were deposited. Gate isolation for the FET wires/fins between different devices (which still had their gates shorted together by the sputtered Cr at this point) and contact holes for the thick gate pads were realized together with an SiO₂ etch followed by a Cr etch.

Finally, a Ti/Al/Pt back contact was deposited with a window left free of metal for collecting light from the back side.

After device processing, electrical and optical measurements were performed, with results for a 500 nm × 50 μm single-fin device shown in Figures 2 and 3, respectively. Circular transfer length method (cTLM) measurements shown in Figure 2(a) reveal low contact and sheet resistances: 9.34 × 10⁻⁶ Wcm² for the top source contact, and 185 Ω/sq for the n⁺⁺GaN contact layer underneath, resulting in negligible voltage drops across these regions. I_D-V_G and I_D-V_D measurements on the 500 nm × 50 μm single-fin device are shown in Figures 2(b) and (c), respectively, with current density values shown on the plots normalized to the area of the finFET.

The measured electroluminescence (EL) spectra are shown in Figure 3, demonstrating the optical modulation enabled by the FinFET. Figures 3(a) and (b) show the effect of the drain voltage on the emission spectra in linear and log scales for the 500 nm × 50 μm single fin device at a fixed V_G = 4V for V_{DS} between 10V and 13V. Figures 3(c) and (d) demonstrate the desired modulation of the EL spectra through gating of the GaN FinFET.

In summary, we have demonstrated a new technique for achieving monolithic integration of n-FETs and LEDs, using vertical fin-and nanowire-FETs and bottom tunnel junction blue LEDs. This platform allows for strong gate control (~ 5 orders of magnitude on/off for I_D) without limiting the on-wafer LED active area, and does not require regrowth.

Optical switching behavior up to 30 kHz is demonstrated in the first prototype, with room for improvement through use of InGaN heterojunction TJs.

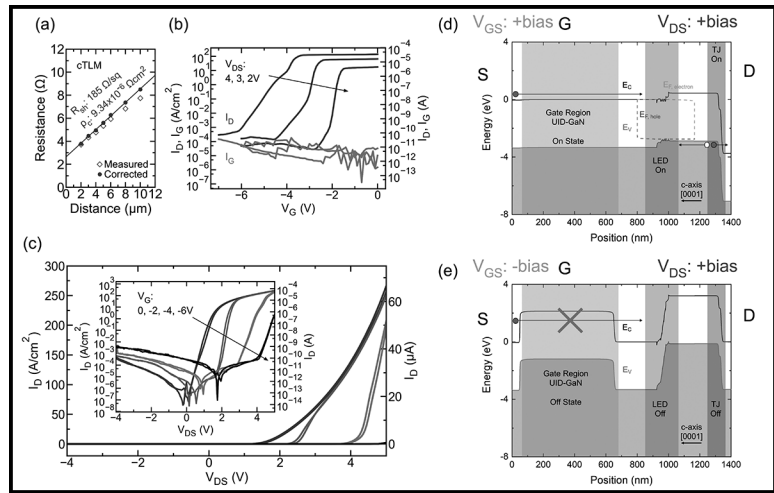


Figure 2: (a) Circular TLM data for the source contact of the LEFET. (b) I_D-V_G measurement for a single-fin device with fin dimensions of 500 nm × 50 μm and LED dimensions of 55 × 55 μm². Current density is calculated using the area of the fin. (c) Linear I_D-V_D characteristic (with log-scale in inset) showing reduction in on current of ~100x at V_{DS} = 5 V as V_G is reduced from 0 V to -6 V. (d), (e) Qualitative depiction of band diagrams for the device in the on and off states, respectively. With a fixed positive V_{DS}, switching V_G from positive to negative biases modulates electron conduction across the FET channel, and allows voltage to drop across the diode.

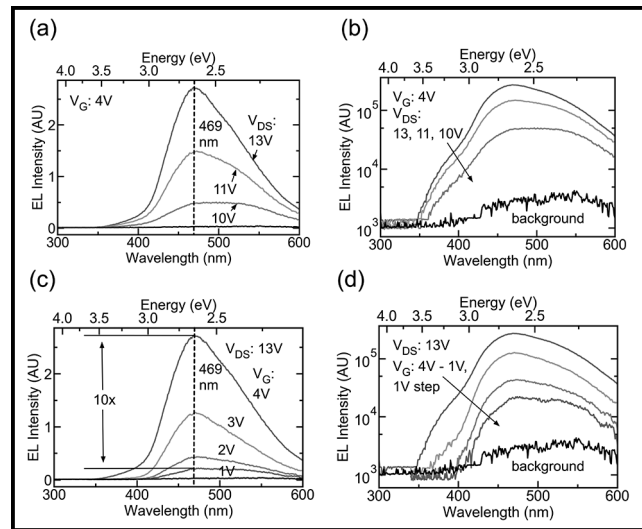


Figure 3: (a), (b) Linear and log scale plots, respectively, of electroluminescence (EL) intensity versus wavelength for a single-fin device, with V_G fixed at +4V. The EL intensity rises as expected with increasing V_{DS} as the level of forward bias across the diode is increased. (c), (d) Linear and log scale plots, respectively, of EL intensity versus wavelength for the same device, with V_{DS} fixed at 13V. A factor of 10 reduction in EL intensity is observed as V_G is decreased from +4V to +1V, demonstrating the gate's ability to limit electron transport into the LED.